Ocean Science
Discussions

Seasonal variability in mass, nutrients and DOC lateral transports off Northwest African Upwelling System

Nadia Burgoa[1], Francisco Machín[1], Ángeles Marrero-Díaz[1], Ángel Rodríguez-Santana[1], Antonio Martínez-Marrero[2], Javier Arístegui[2], and Carlos M. Duarte[3]

[1]Departamento de Física, Universidad de Las Palmas de Gran Canaria, Spain
[2]Instituto de Oceanografía y Cambio Global, Universidad de Las Palmas de Gran Canaria, Spain
[3]Red Sea Research Center, King Abdullah University of Science and Technology, Saudi Arabia

Correspondence: Nadia Burgoa (nadia.burgoa@ulpgc.es)

Abstract.

The Coastal-Ocean Carbon Exchange in the Canary Region Project (COCA) arises in order to analyse and get to understand the impact of lateral export of nutrients and organic matter from the highly productive Coastal Upwelling System off NW Africa in the biogeochemical cycles during two different seasons.

5   The circulation patterns off NW African Upwelling System are examined by applying an inverse model to two hydrographic datasets gathered in fall 2002 and spring 2003. The mass transports estimated by model are consistent with the thermal wind equation and the conservation of mass in a closed volume. Besides, the Ekman transport and the freshwater flux are also considered.

These estimates show a seasonal variability in the circulation patterns at central levels, particularly in the southern boundary

10   of the domain, where the Cape Verde Frontal Zone is located. In the beginning of fall, this circulation is deeper and northward with a net transport of 6 ± 3 Sv and, in the late spring, it is shallower and southward with a similar intensity. At intermediate levels important differences are also observed between the two seasons. In fall, the Antarctic Intermediate Waters reaches higher latitudes with 2 ± 2 Sv flowing northward. During spring, there is no significant northward flow of AAIW. However, there is a moderate westward mass transport which impacts both the lateral transports of inorganic nutrients and organic matter

15   at intermediate layers and also the shallowest lateral transports of organic matter.

Seasonal variability in circulation patterns are also reflected in lateral transports of inorganic nutrients and dissolved organic carbon. Therefore, the changes in the circulation patterns between the two seasons have allowed us to assess the variability in the contributions of SiO_2, NO_3, PO_4 and DOC from the first to the second season. In fall, the transports are mainly northward from the south with -0.80 ± 0.34, -1.11 ± 0.47 and $-0.07 \pm 0.03 \, \mathrm{kmol \, s^{-1}}$ of SiO_2, NO_3 and PO_4, respectively.

20   In spring, however, lateral transports off-shore are favoured with 0.75 ± 0.37, 1.34 ± 0.66 and $0.08 \pm 0.04 \, \mathrm{kmol \, s^{-1}}$ of SiO_2, NO_3 and PO_4, respectively. This westward transport stimulates in turn an intensified westward DOC transport at shallow layers, specifically $0.50 \pm 0.25 \times 10^8 \, \mathrm{mol \, C \, day^{-1}}$.

1   INTRODUCTION

The North Atlantic Subtropical Gyre (NASG) is one of the most important components in the thermohaline circulation. It presents a well-known intensification in its western margin, the Gulf Stream, with maximum velocities up to $2\,\mathrm{m\,s^{-1}}$ (Halkin et al., 1985). The currents observed in this western margin of the gyre occupy a small horizontal extension as compared to that of the currents in the eastern side, resulting in an asymmetric gyre (Stramma, 1984; Tomczak and Godfrey, 2003). The low intensity of the currents at the eastern boundary made them very little studied until the 1970s, when CINECA program focused on the productive African upwelling (Ekman, 1923; Tomczak, 1979; Hughes and Barton, 1974; Hempel, 1982). Käse and Siedler (1982) found striking intense currents south of the Azores connected to the Gulf Stream and suggested that part of the recirculation of the NASG occurs southward in the vicinity of the African coast. Later on, several surveys based on both *in situ* and remote sensing observations contributed to define the general characteristics for the average flow of the region (Käse and Siedler, 1982; Stramma, 1984; Käse et al., 1986; Stramma and Siedler, 1988; Mittelstaedt, 1991; Zenk et al., 1991; Fiekas et al., 1992; Hernández-Guerra et al., 1993).

Most of the eastward flow from the Gulf Stream is confined to a band between the Azores and Madeira Islands, recirculating southward through the Canary Islands and north of the Cape Verde Islands to become into a southwestward flow (Stramma, 1984). This current system is composed by the Azores Current (AC), the Canary Current (CC), the Canary Upwelling Current (CUC), the North Equatorial Current (NEC) and the Poleward Undercurrent (PUC). The AC divides into several branches defining the boundary current system off Northwest Africa. It firstly feeds the Iberian Current (Haynes et al., 1993) while a second significant branch enters the Mediterranean Sea (Candela, 2001). Most of the AC recirculates southward splitting into the main CC across the Canarian archipelago and the secondary CUC (Pelegrí et al., 2005, 2006). These currents extend southward developing the Cape Verde Frontal Zone (CVFZ), a density-compensated front with North Atlantic Central Water at its northern side and South Atlantic Central Water at its southern one (Zenk et al., 1991; Martínez-Marrero et al., 2008). Finally, the PUC is located below the CUC flowing northward on the continental slope (Barton, 1989; Machín and Pelegrí, 2009; Machín et al., 2010; Pelegrí and Peña-Izquierdo, 2015).

The mesoscale activity constitutes a second main feature in the area of interest, which might be even more energetic than the average flow itself (Sangrà et al., 2009). Three mesoscale domains may be defined: the Canary Eddy Corridor (CEC, Sangrà et al. (2009)), the CVFZ and the upwelling front. The CEC is located downstream of the Canary Islands where the interaction between the southward flow and the archipelago generates long-lived eddies (Arístegui et al., 1994; Barton et al., 1998; Sangrà et al., 2007, 2009; Ruiz et al., 2014; Barceló-Llull et al., 2017a). The second mesoscale domain is the CVFZ, where several meanders and eddies produce strong interleaving between the water masses involved (Pérez-Rodríguez et al., 2001; Martínez-Marrero et al., 2008). In this domain, the CC and the CUC separate from the African coast fueling the NEC, giving rise to a shadow zone featured by poorly ventilated waters (Luyten et al., 1983). The third area is the front arising between the coastal upwelled waters and the stratified interior waters, defining the Eastern Boundary Upwelling System (EBUS) in the Northwest African region (Mittelstaedt, 1983; Pastor et al., 2008; Arístegui et al., 2009). This EBUS is actually located off the African slope from the Gulf of Cadiz until Cape Blanc/Cape Verde in summer/winter with a high mesoscale vari-

ability in the form of both filaments and eddies (Hagen, 2001; Sangrà et al., 2009; Ruiz et al., 2014). The upwelling process raises nutrient-rich waters to the euphotic layer, developing a high primary production latitudinal band off Northwest Africa known as the Coastal Transition Zone (CTZ) (Barton et al., 1998; Pelegrí et al., 2006). The mesoscale activity plays an essen-

60   tial role as a lateral source of nutrients and organic matter towards the oligotrophic waters of the NASG (Barton et al., 1998; García-Muñoz et al., 2004; Pelegrí et al., 2006; Álvarez-Salgado et al., 2007; Sangrà et al., 2009).

The distribution of inorganic nutrients and organic matter in the ocean responds to a combined effect of physical and biogeochemical processes. Within the euphotic zone, primary production is solely limited by the availability of inorganic nutrients (IN) (Copin-Montegut and Copin-Montegut, 1983; Falkowski et al., 1998). Below the euphotic zone respiration generally ex-

65   ceeds primary production. As a result, the organic matter produced at the sea surface is remineralized in the subsurface layers and hence the concentration of IN increases from the interplay between the local rate of remineralization and the rate of water supply (Azam, 1998; Del Giorgio and Duarte, 2002; Pelegrí et al., 2006; Pelegrí and Benazzouz, 2015b).

The relevance of lateral advective transports on the spatio-temporal distribution of biogeochemical variables in the ocean has historically received little attention (Ganachaud, 1999; Ganachaud and Wunsch, 2002b). Specifically in the EBUS off North-

70   west Africa, some recent manuscripts related to lateral advective transports of biogeochemical variables have shed light on this topic (Álvarez and Álvarez-Salgado, 2009; Alonso-González et al., 2009; Santana-Falcón et al., 2017; Fernández-Castro et al., 2018).

The ocean dynamics in the region between $10°$ and $40°$N off Northwest Africa during two different seasons is addressed in this manuscript. An inverse box model is applied to hydrographic observations to estimate mass transports. This method

75   provides a velocity field consistent with both mass and properties conservation within a closed volume and with the thermal wind equation (Wunsch, 1996). Several authors have already described the circulation patterns of the NASG by applying an inverse model (Ganachaud and Wunsch, 2002a; Ganachaud, 2003b, a; Hernández-Guerra et al., 2005; Machín et al., 2006; Pérez-Hernández et al., 2013; Hernández-Guerra et al., 2017).

To sum up, the main goal of this manuscript is to estimate mass, nutrient and organic matter transports during fall and spring

80   south of the Canary Islands in the context of a highly variable environment as the CVFZ. The remaining of this manuscript is organized as follows: the dataset is presented in section 2; the seasonal distribution of the water masses and their properties is displayed in section 3; the technical details of the inverse box model are covered in section 4; the resulting velocity field and the corresponding mass, nutrient and organic matter transports are presented in section 5. Section 6 is devoted to the discussion to end up with some conclusions at section 7.

85   ## 2   DATASET

COCA-I and COCA-II cruises were carried out in fall (10 September to 1 October 2002) and spring (21 May to 7 June 2003) respectively, aboard the BIO Hesperides as part of the research project Coastal-Ocean Carbon Exchange in the Canary Region (Hernández-León et al., 2019). The location of Conductivity-Temperature-Depth (CTD), inorganic nutrients (IN) and dissolved organic carbon (DOC) stations in COCA-I and COCA-II defines a closed box along three transects (Figure 1). The northern

Ocean Science
Discussions

90   transect (N) spans from station 1 to 32 at $26°$N (section from stations 1 to 11 is tilted some $30°$ with respect to the east). The
       western transect (W) is located at $26°$W from station 32 to 42. Finally, the southern zonal transect (S) at $21°$N runs from station
       42 to 63 (COCA-I) or 66 (COCA-II) over the continental slope (Table 1). The distance between neighbouring CTD stations
       was some 50 km except for the stations over the continental slope where this distance was shortened. Adjacent DOC and IN
       stations were separated by a variable distance, with its lowest value being about 50 km at stations closer to the coast.

95   CTD data were collected from the sea surface down to 2000 m depth with a vertical resolution of 2 dbar. Temperature
       was calibrated with 45 readings performed with a reversible digital thermometer, while salinity was calibrated by analysing 60
       water samples with the Portasal salinometer. The residuals have an average value of 0.00013 ± 0.00400 °C and 0.0005 ± 0.005
       in salinity.

       Total organic carbon (TOC) was analyzed assuming that it is virtually in dissolved form. Water samples (10 mL) were
100   dispensed directly into glass ampoules, previously combusted at 500 °C during 12 h. 50 µL of H_3PO_4 were added immediately
       to the sample, sealed and stored at 4 °C until analyzed with a Shimadzu TOC-5000 (Sharp et al., 1993). Before the analysis,
       samples were sparged with CO_2-free air for several minutes to remove inorganic carbon. TOC concentrations were determined
       from standard curves (30 to 200 µM) of potassium hydrogen phthalate produced every day (Thomas et al., 1995). To check
       accuracy and precision, reference material from Jonathan H. Sharp laboratory (University of Delaware) was analyzed daily.
105   DOC distribution up to 2000 m depth presented a more representative coverage in fall than in spring (Fig. 2, green dots),
       despite in spring the number of stations was higher than in fall (Fig. 1, black circles; Tab. 1).

       The three inorganic nutrient sampled were silicates (SiO_2), nitrates plus nitrites (NO_x), and phosphates (PO_4). These sam-
       ples were frozen until measured with a Bran Luebe AA3 autoanalyser following the standard methodology established by
       Hansen and Koroleff (1999). Nutrient data covered up to 2000 m, while in fall they concentrated in the shallowest layers
110   (< 200 m, Fig. 2, pink crosses).

       Wind data were selected from the QuikSCAT database made available by CERSAT (Centre ERS d' Archivage et de Traite-
       ment, http://www.ifremer.fr/cersat/). These wind fields were averaged weekly with a spatial resolution of $0.5°$ (shown in Fig. 1
       with half of the original spatial resolution). The Smith-Sandwell database with 1-minute horizontal resolution was used as the
       source of bathymetry data (Smith and Sandwell, 1997).

115   Freshwater flux data were estimated from the rates of evaporation and precipitation extracted from the Surface Marine
       Data 1994 of Da Silva (http://iridl.ldeo.columbia.edu/SOURCES/.DASILVA/.SMD94/). The climatological mean depths of
       the neutral density field for the years 2002 and 2003 were calculated from the climatological temperature and salinity extracted
       from the World Ocean Atlas 2013 (WOA13, https://www.nodc.noaa.gov/OC5/woa13/woa13data.html).

       GLORYS (GLOBAL_REANALYSIS_PHY_001_025 product) issued by Copernicus Marine Environment Monitoring Ser-
120   vice (CMEMS, http://marine.copernicus.eu) was used as a primary source of dynamic variables. Its horizontal resolution is
       $1/12°$ with 50 standard depths. Hydrological data from GLORYS were also employed to diagnose the average oceanographic
       conditions during each cruise. This product assimilates field observations in real time.

Ocean Science
Discussions

SEALEVEL_GLO_PHY_L4_REP_OBSERVATIONS_008_047 product provided surface geostrophic currents estimated from sea level anomalies. These data capture the mesoscale structures and are helpful to validate the near-surface geostrophic
125 field estimated from the inverse model.

GLORYS-BIO (GLOBAL_REANALYSIS_BIO_001_029 product) produced daily mean 3D biogeochemical fields with the same resolution as GLORYS. This reanalysis forces the biogeochemical model with the nutrient initial conditions from WOA13. IN concentrations from GLORYS-BIO (SiO_2, NO_3, and PO_4) were used to assess nutrient transports by the model (in section 5).

130 The data treatment, the graphical representations and the inverse model are coded in MATLAB (MATLAB, 2018). The vertical sections are produced using the 'nearest' 2D interpolations, a method also employed in the estimates of the IN and DOC transports. Ocean Data View using the DIVA gridding method is employed to produce DOC concentration charts (Schlitzer, Reiner, 2019).

3   HYDROGRAPHY AND WATER MASSES

135 Neutral density $\gamma_n = \gamma_n(\theta, S, p)$ is used as the density reference variable, being the isoneutrals the surfaces where value of γ_n is constant (Jackett and McDougall, 1997). The γ_n vertical sections contain the surface (SW), central (CW), intermediate (IW) and deep water (DW) masses according to Macdonald (1998) for the North Atlantic at 24°N, represented with white dashed lines at 26.44, 27.38 and 27.82 $\mathrm{kg\,m^{-3}}$ (Figure 2). The x-axis direction is selected according to the path followed by the vessel during both cruises, starting in the northeast and finishing in the southeast of the domain. The N/W and W/S corners
140 are indicated with two vertical grey dashed lines at stations 32 and 42, respectively.

The $\Theta - S_A$ diagrams exhibit four regions delimited by potential density anomaly contours of 26.39, 27.30 and 27.72 $\mathrm{kg\,m^{-3}}$, equivalent to the isoneutrals which separate the main water masses (Fig. 3). These three isoneutrals are approximately at 132/123, 672/700 and 1294/1305 m depth (Fig. 2). The water masses sampled during both cruises are North Atlantic Central Water (NACW), South Atlantic Central Water (SACW), Antarctic Intermediate Water (AAIW), Mediterranean Water (MW),
145 and North Atlantic Deep Water (NADW) (Emery and Meincke, 1986; Macdonald, 1998; Emery, 2008). Their main hydrological characteristics are summarized in Table 2. Below the mixing layer and above 700 m ($26.44 < \gamma_n < 27.38\,\mathrm{kg\,m^{-3}}$), NACW and SACW are the dominant water masses. SACW is featured by a higher amount of nutrients, $1 - 2\,°C$ colder and $0.1 - 0.4$ fresher than NACW (Fig. 3 and Tab. 2). Below, from 700 up to 1300 m ($27.38 < \gamma_n < 27.82\,\mathrm{kg\,m^{-3}}$), the intermediate waters AAIW and MW are the dominant water masses (Hernández-Guerra et al., 2017). MW is a relatively warm and salty water
150 mass, while AAIW is colder and fresher (Tab. 2). Finally, below 1300 m ($\gamma_n > 27.82\,\mathrm{kg\,m^{-3}}$) the predominant water mass is NADW with *in situ* temperature and salinity values lower than $5.7\,°C$ and 35.14 (Tab. 2).

A description about the seasonal variability of the water masses is also performed with observations from the $\Theta - S_A$ diagrams (Fig. 3). The distribution of water masses is quite similar for both cruises. There is a higher temperature variability at surface waters during fall with maximum values 2-3 ºC higher than in spring. During spring, the variability observed at central
155 waters is associated to larger fluctuations in salinity affecting the whole water column. At DW there is a higher contribution of

Ocean Science
Discussions

NADW in the whole domain during fall. Finally, the surface layer is thicker in fall than in spring in all the sections made with respect to γ_n.

These seasonal differences may also be described transect to transect. The northern transect (Fig. 2, stations 2 to 32; Fig. 3, margenta dots) is occupied by NACW, AAIW, MW and NADW in both seasons. At intermediate levels, a higher contribution
160 of MW is observed in spring while a slightly higher contribution of AAIW is obtained in fall. The western transect (Fig. 2, stations 32 to 42; Fig. 3, dark grey dots) has a similar distribution as the northern one, with a lower variability in the upper layers and a smaller influence of MW. In the southern transect (Fig. 2, stations 42 to $63 - 66$; Fig. 3, blue dots), the highest spatio-temporal variability is observed. This variability at surface and central levels is associated to the position of the CVFZ and, in turn, to the meso- and submesoscale structures associated to the front. The CVFZ is located where the isohaline of 36,
165 or equivalently $S_A = 36.15 \text{ g kg}^{-1}$, intersects the 150 m isobath (Zenk et al., 1991) (Fig. 4). CVFZ is found in the southern transect in its westernmost position in fall, at stations $46 - 48$. Hence, SACW with relatively low S_A is observed above the upper limit of CW east of the CVFZ location (Fig. 4). In spring, the CVFZ shifts to a position closer to the African coast at station 52, with a water incursion of higher salinity NACW centred at station 58 (Figs. 4 and 5). At intermediate levels, MW is registered at the northern transect while in the southern one the predominant water mass is AAIW. Regarding the seasonal
170 variability, the contribution of MW in the northern transect is higher in spring while the contribution of AAIW in the southern transect is higher in fall.

Although the IN have been extracted from the model and the distributions of Θ, S_A and γ_n have been obtained from the hydrographic data, there is a good agreement between the structures described by both datasets. The *in situ* concentrations of SiO_2, NO_X and PO_4 up to 250 m depth (black dots in Fig. 6) are represented together with the time-averaged concentrations
175 of SiO_2, NO_3 and PO_4 up to 2000 m depth selected from GLROYS-BIO. In this way the IN outputs from the model are compared with *in situ* observations since their concentration in both cases present an acceptable match with the exception of NO_X and PO_4 concentrations at the S transect. On the other hand, the IN model outputs look alike IN from historical *in situ* databases (not shown here).

At central levels, high IN concentrations have been sampled near the continental slope in both the northern (stations 10 to 18)
180 and southern (50 to 56) transects in fall. Values observed are 1-5 $\mu\text{mol kg}^{-1}$ for NO_3 and 0.1-0.4 $\mu\text{mol kg}^{-1}$ for PO_4 higher than those recorded in spring at similar places (Fig. 7). This might be related to long-lived mesoscale eddies or instabilities related to the CVFZ (Zenk et al., 1991; Sangrà et al., 2009). IN concentrations are notably high at intermediate and deep levels as compared to those at central levels (Fig. 6) and have the same order of magnitude as those documented before in the domain (Pérez et al., 2001; Pérez-Hernández et al., 2013). The distributions of SiO_2, NO_3 and PO_4 are similar in both cruises and
185 their concentrations increase with depth as a result of the remineralization of organic matter (Fig. 7). The area where the least nutrients are found at depth throughout the domain is the northwest corner of the box (stations 24 to 32). With respect to the IN seasonal variability at intermediate depths, the three concentrations do not present large differences between the values measured in fall and spring (Figs. 7 and 3). In both seasons the concentrations of SiO_2, NO_3 and PO_4 are 4-6, 2-6 and 0.2-0.4 $\mu\text{mol kg}^{-1}$ higher in AAIW than in MW (Tab. 2). The NADW is characterized by a moderate increase of SiO_2 and by
190 a slight decrease of NO_3 and PO_4 with respect to the values documented here at intermediate levels. In both seasons, the

maximum concentrations of SiO_2 are 28-29 $\mu mol\,kg^{-1}$. Nevertheless, and specifically in spring, maximum concentrations of NO_3 and PO_4, 28 $\mu mol\,kg^{-1}$ and 1.8-1.9 $\mu mol\,kg^{-1}$, are lower than those recorded at intermediate levels, providing a similar vertical variability as that reported by Machín et al. (2006) (Tab. 2).

DOC concentrations are higher and more widely distributed in the water column in fall than in spring, when the DOC maximum values are more confined to surface and central waters (Figs. 8 and 6, Tab. 2). This fact is especially significant in the southern transect occupied by SACW (Fig. 6). This last water mass presents maximum concentrations of DOC $35 - 40$ $\mu mol\,L^{-1}$ lower than those found for NACW (Tab. 2). This difference is more pronounced in spring season (Tab. 2). In addition, the fall DOC observations present a larger variability in central waters as previously seen for IN. Lower DOC concentrations are observed for stations sampled in the western transect while the highest concentrations are recorded in the stations next to the African slope with values above 100 $\mu mol\,L^{-1}$ (Fig. 8). On the other hand, it is noteworthy the high concentrations of DOC recorded at intermediate waters of the northern transect in both cruises (Figs. 8 and 6).

4 THE INVERSE MODEL

An inverse box model is applied to the hydrographic data of the two COCA cruises to provide the absolute velocity field across the three sections (Wunsch, 1978). This method has been widely applied in different areas of the Atlantic Ocean as an efficient method to obtain absolute geostrophic flows (Martel and Wunsch, 1993; Paillet and Mercier, 1997; Ganachaud, 2003a; Machín et al., 2006; Pérez-Hernández et al., 2013; Hernández-Guerra et al., 2017; Fu et al., 2018). Assuming geostrophy and the conservation of mass and other properties in the ocean bounded by the African coast and the hydrological sections, the velocity fields are obtained allowing an adjustment of freshwater flux and Ekman transports.

4.1 Selection of layers

The closed ocean where the inverse model is applied is divided into nine layers by means of the neutral densities defined by Macdonald (1998) and modified by Ganachaud (2003a) for the North Atlantic Ocean. This distribution is slightly modified to include two layers instead of one between 26.85 and 27.162 $kg\,m^{-3}$ by adding the isoneutral 27.035 $kg\,m^{-3}$ as others authors have done previously in this side of the NASG (Comas-Rodríguez et al., 2011; Pérez-Hernández et al., 2013). The location of the isoneutrals are represented in Figure 2. The upper five layers group the surface and central waters, with the first layer until the isoneutral 26.44 $kg\,m^{-3}$ being related to surface waters and the 4 remaining layers between 26.44 $kg\,m^{-3}$ and 27.38 $kg\,m^{-3}$ to central waters. The intermediate waters are found in the next two layers between 27.38 and 27.82 $kg\,m^{-3}$ while the deepest two layers below 27.82 $kg\,m^{-3}$ contain the upper deep waters.

4.2 The system of equations

The inverse box model takes into account mass conservation per layer and also in the whole water column. The salinity is actually introduced as a salinity anomaly, which is also conservative within individual layers and in the whole water column (Ganachaud, 2003b). On the other hand, heat is introduced as a heat anomaly in the two deepest layers where it is also

considered conservative. The salinity and heat are added as anomalies to improve the conditioning of the inverse model and get a higher rank in the system of equations by reducing the linear dependency between equations (Ganachaud, 2003b).

Therefore, the model is composed of a set of 22 equations (10 for mass conservation, 10 for salt anomaly conservation and

225   2 for heat anomaly conservation). Those equations are solved for 32 and 34 unknowns, comprised of $28/30$ reference level velocities in fall/spring, 3 unknowns for the Ekman transport adjustments (one unknown per section), and 1 unknown for the freshwater flux. The resulting system is undetermined and a Gauss-Markov estimator is used to select a solution by adding *a priori* information. This *a priori* information consists of the uncertainties for both the unknowns (R_{xx}) and the noise of the equations (R_{nn}).

4.2.1   Uncertainties of unknowns (R_{xx})

230

The geostrophic velocity field is calculated in the central position between two consecutive stations. The isoneutral selected as the reference level is the deepest common γ_n for all the stations, $27.962\,\mathrm{kg\,m^{-3}}$ (Fig. 2). The variance of the velocity in the reference level at each location is used as a measure of the *a priori* information. These variances are calculated with an annual mean velocity extracted from the daily velocity provided by GLORYS. These velocities are interpolated to the reference level

235   depth. This reference level depth is estimated from the climatological mean depth of $27.962\,\mathrm{kg\,m^{-3}}$ extracted from WOA13. The stations closer to the coast in the northern and southern transects have the highest variability in the velocity field.

The initial Ekman transports are estimated from the wind stress for both cruises. The uncertainty associated to these Ekman transports is related to the error in their measurements and to the variability of the wind stress. A 50% uncertainty is assigned to the initial estimate of Ekman transports. The initial freshwater flux is a climatological mean of 0.0171 Sv, which is also assigned

240   an uncertainty of $50\,\%$ as reported in similar approaches (Ganachaud, 1999; Hernández-Guerra et al., 2005; Machín et al., 2006).

Both the Ekman transports and freshwater flux with their uncertainties are added to the model in the conservation equations corresponding to the shallowest layer of the mass transport and salt anomaly and also in the conservation equations of total mass transport and total salt anomaly.

4.2.2   Uncertainties in the noise of equations (R_{nn})

245

The noise of each equation depends on the density field, on the layer thickness and on the uncertainties of the unknowns (Ganachaud, 1999, 2003b; Machín et al., 2006). In fact, Ganachaud (2003b) established that the largest source of uncertainty in conservation equations arises from the deviation of the baroclinic mass transport from their mean value at the time of the cruise. Thus, an analysis of the annual variability in the velocity field for the nine layers is performed. The velocity variability

250   is examined in the mean depth between two successive isoneutral surfaces whose climatological mean depths are defined by WOA13. These variabilities are included in the inverse model as the uncertainties of the *a priori* noise of equations in terms of variances of mass, salt anomaly and heat anomaly transports. The velocity variance from the annual mean velocity for each layer are estimated with GLORYS and transformed into transport values by multiplying times density and the vertical area of

the section involved. These *a priori* transport uncertainties are presented in Table 3. Furthermore, the uncertainty assigned to
255 the conservation equation in the total mass is the sum of the uncertainties from the rest of the nine conservative mass equations.

The equations for salt and heat anomaly conservation depend on both the uncertainty of the mass transport and the variance
of these properties (Ganachaud, 1999). In these cases, the *a priori* noise of each equation will not depend strictly on the water
mass but on the layer considered, as shown in the following equation (Ganachaud, 1999; Machín, 2003):

$$R_{nn}(Cq) = a * var(C_q) * R_{nn}(mass(q)) \tag{1}$$

260 where $R_{nn}(Cq)$ is the uncertainty in the anomaly equation of the property (salt or heat anomaly); $var(C_q)$ is the variance
of this property; a is a weighting factor of 4 in the heat anomaly, 1000 in the salt anomaly and 10^6 in the total salt anomaly; q
is a given equation corresponding to a given layer.

5 RESULTS

5.1 Velocity fields and mass transports

265 Figure 9 shows the reference level velocities obtained after the inversion is performed. The variance of these velocities are
also estimated by the model. The uncertainties are much higher than the values themselves and around $\pm$ (0.5-1) $\mathrm{cm\,s^{-1}}$.
During fall all non-zero values are positive, while in spring they are negative. This difference is important mainly in the
western and southern transects where the module of the velocity increases reaching values of 0.3 and -0.16 $\mathrm{cm\,s^{-1}}$ in fall
and spring, respectively. Furthermore, the estimated reference level velocity values in the northern transect in spring are too
270 small, $O(10^{-4}-10^{-5})$, while they take positive and significant values between 0.13 and 0.25 $\mathrm{cm\,s^{-1}}$ in some locations of this
transect in fall.

Once the geostrophic velocities at the reference level are estimated, they are integrated into the entire water column obtaining
the absolute geostrophic velocities (Fig. 10). These results are validated by comparison with the surface geostrophic velocity
and the sea level anomaly (SLA) derived from altimetry during both cruises (Fig. 11). To do this, the average fields of SLA and
275 geostrophic velocity at the sea surface are calculated and shown as a representation of the synoptic situation during both sur-
veys. Furthermore, the mass transports at the shallowest layer (red bars in Fig. 11), are superimposed with the aim of comparing
these transports with the average velocity field from altimetry. A remarkable mesoscale activity can be identified at both the
absolute geostrophic velocity sections (Fig. 10) and at the temporal average of SLA and the geostrophic velocity (Fig. 11). In
this last case, the structures are somewhat displaced with respect to their positions in the *in situ* velocity sections. For instance,
280 an anticyclonic eddy is located between stations 10 and 16 in the N transect in both seasons. This eddy, observed in autumn
with high velocities at intermediate layers, weakens in spring. This mesoscale structure could be part of the CEC (Sangrà et al.,
2009). Furthermore, it coincides with the position of an anticyclonic eddy previously documented (Barceló-Llull et al., 2017a;
Barceló-Llull et al., 2017b; Estrada-Allis et al., 2019).

In fall, two eddies are linked in the S transect, an anticyclonic one between stations 48 and 52 and a cyclonic one between
285 stations 52 and 60, both associated with the CVFZ. In spring, two anticyclonic eddies are observed, one centred at station

Ocean Science
Discussions

36 and the other one at station 56 also associated with CVFZ. In both seasons, mesoscale structures present a large vertical extension (Figure 10). In fall, these structures have higher velocities at IW and DW levels and they also affect a higher extension along each transect. In spring instead, these structures are vertically shortened (Fig. 10). The SLA also shows a high variability region with more intense structures in fall than in spring (Fig. 11).

290   Mesoscale structures are also visible in the vertical sections of NO_3 and PO_4 in fall, when their concentrations are higher than those observed in spring at similar locations (Fig. 7). Furthermore, high concentrations of DOC in fall at CW levels are recorded in the same area where the deep anticyclonic eddy is located, between stations 8 and 18 (Fig. 8). In spring, mesoscale structures in the vertical sections of IN and DOC at CW levels are less intense than in fall (Fig. 10). Nonetheless, DOC concentrations below the two anticyclonic structures at CW levels in spring are higher than at their surroundings.

295   The accumulated geostrophic mass transport is integrated to group the variability at different levels, having the first shallowest layer for SW, the next four layers for CW, then two layers for IW and the deepest two layers for DW (Figure 12). The total accumulated geostrophic mass transport, integrated for all the nine layers, is also represented. The horizontal axis has the same direction as the rest of the vertical sections and the three transects are separated by two vertical dashed grey lines. Sv is used here as equivalent to $10^9 \, \mathrm{kg \, s^{-1}}$. The positive/negative transport values indicate outward/inward transports from/to the box.

300   The accumulated mass transports show a significant horizontal spatial variability, especially marked in the southern transect in accordance to the geostrophic velocity distribution (Fig. 10). The presence of significant mesoscale structures might be one of the sources for the total imbalances in the accumulated mass transport. In fall, the total imbalance is -1.43 Sv and in spring 3.55 Sv (Tab. 4).

On the other hand, the geostrophic mass transport can be integrated per layer and transect together with the total imbalance

305   inside the box and the total mass transport uncertainty per layer (black line and horizontal black bars in Fig. 13). Moreover, Table 4 compiles these transports integrated for the different water levels. More than 65% of the mass transport is given at SW and CW levels (Tab. 4). In fall, these water masses mostly get into the box across the northern and southern transects with transports of -5.61 ± 1.86 Sv and -4.35 ± 1.48 Sv, respectively; the mass leaves the box by flowing westward with a value of 5.96 ± 1.75 Sv. In spring, water masses also get in the box mostly through the northern transect with -6.69 ± 1.63 Sv but

310   they set off along the western and southern transects with transports of 4.05 ± 1.75 Sv and 5.20 ± 1.55 Sv, respectively. It is remarkable how the inward transport in fall across the southern transect is reversed to an outward flow in spring at the southern transect (Fig. 13).

The position of CVFZ in both seasons could partly explain that seasonal variability in the mass transports at central levels (Fig. 14). In fall, the CVFZ is located further from the African coast, so SACW is present at almost all stations of the south

315   transect. This location of the CVFZ prevents a latitudinal mass transport from north to south. However, in spring the CVFZ is closer to the African slope allowing an important mass transport from north to south.

Between 5 and 30% of the mass transport is given in intermediate levels (Tab. 4). In fall, the intermediate water transport directs northward in the southern transect with -1.93 ± 1.69 Sv and it leaves the box with 1.94 ± 1.85 Sv and 0.48 ± 1.71 Sv across the northern and western transects, respectively. During spring, this transport weakens and changes its direction in the

Ocean Science
Discussions

320   northern and southern transects with transports of -0.48 ± 1.65 Sv and 0.39 ± 1.73 Sv, respectively, increasing its westward

transport to 1.21 ± 1.68 Sv.

The mass transport in deep water layers barely exceeds 3% (Tab. 4). An exception is the 8% given in the northern transect

during fall where the estimated transport is 0.73 ± 1.71 Sv. In both cruises the transport at deep levels is nearly balanced.

5.2   Nutrient and DOC transports

325   DOC and IN transports are obtained by multiplying their concentration times mass transports. DOC, IN and geostrophic

velocities are obtained at different grids, so they need to be interpolated to the same grid. In the case of DOC, the velocities

are interpolated to the points where the concentrations of DOC are taken and, in a second step, the concentrations of DOC are

linearly interpolated to the depths of the geostrophic velocities. On the other hand, the *in situ* measurements of IN are scarce

at IW and DW where their concentrations become important. Therefore, instead of using the observational data, the average

330   outputs of GLORYS-BIO are used to estimate the IN transports. SiO_2, NO_3, and PO_4 mean concentrations are interpolated to

the grid nodes where the geostrophic velocities are estimated by the inverse model.

DOC transports are obtained by subtracting a refractory concentration of $40 \, \mu mol \, L^{-1}$ from the measured DOC as other

authors do (e.g., Santana-Falcón et al., 2017). This is done because the refractory fraction renewal is thousands of years, a

period much longer than the time required in the processes we are focused on (Hansell, 2002). On the other hand, it should be

335   emphasized that DOC transports may be underestimated due to the scarcity of measurements performed.

The IN transport values are being presented in the text always ordered as SiO_2, NO_3 and PO_4 (Figures 15 and 16). Tables 5,

6 and 7 summarize those transports integrated per water level and transect. The errors are relative to the mass transport errors

and are calculated as the standard deviations of IN transports. On the other hand, the DOC transport estimates per layer and

transect are also shown in Figure 16 and summarized per water level and transect with their relative error (calculated as in the

340   IN transports) in Table 8. In order to be able to compare our transport values of IN and DOC with those reported by other

authors, units of $kmol \, s^{-1}$ and $\times 10^8 \, mol \, C \, day^{-1}$ are employed for IN and DOC transports, respectively, being both units

equivalent.

IN enter the domain both from north and south at CW in fall. At the northern transect the transports are relatively low while at

the southern one transports double the amount coming from north, with -0.41 ± 0.11, -0.78 ± 0.21 and $-0.05 \pm 0.01 \, kmol \, s^{-1}$.

345   In spring, instead, the IN transports change their direction in the southern transect and only enter from the north with values

which double those during fall, -0.40 ± 0.09, -0.90 ± 0.21, $-0.06 \pm 0.01 \, kmol \, s^{-1}$. On the other hand, IN transports at CW

layers are overall westward with low values in fall while in spring IN transports are southward and westward.

At IW levels, during fall the IN transports are inward through the southern transect with -0.27 ± 0.24, -0.36 ± 0.32,

and $-0.02 \pm 0.02 \, kmol \, s^{-1}$, and to a lesser extent through the western transect. Outward transports are observed through

350   the northern transect with 0.23 ± 0.22, 0.30 ± 0.28 and $0.02 \pm 0.02 \, kmol \, s^{-1}$. In spring, the IN enter weakly through the

northern transect and leave the box crossing the western and southern transects with significant values of 0.19 ± 0.27 and

$0.12 \pm 0.55 \, kmol \, s^{-1}$ for SiO_2; 0.25 ± 0.35 and $0.17 \pm 0.75 \, kmol \, s^{-1}$ for NO_3; and 0.02 ± 0.02 and $0.01 \pm 0.05 \, kmol \, s^{-1}$

Ocean Science
Discussions

Open Access

for PO_4. In summary, while in fall the main IN transports are in the south to north direction, in spring they are mainly southwestward like the mass transport behaviour at these levels during this season (Tab. 4).

355   Finally, at DW during both seasons, the net transports of the three nutrients are similar to those at IW but with smaller values due to the low velocities at these depths, despite their high nutrient concentrations (Figs. 15 and 16). Furthermore, the relative error in these layers is always larger than the IN transport values.

In spring, DOC transports at SW and CW levels are the same order of magnitude and one order of magnitude higher than those at IW levels. In turn, these transports at IW levels are one order of magnitude higher than those at DW levels during this

360   season. In contrast, during fall at the northern transect DOC transports have the same magnitude in both SW, CW and IW and they are one order of magnitude smaller than those at CW levels during spring (Tab. 8). In this season, DOC transports at SW and CW of the western transect have unrealistic small values likely related to the low amount of measurements made in this transect during fall. DOC transports through the northern transect could also be somewhat underestimated for the same reason. However, at the southern transect during fall, the result is of the same order of magnitude as in spring.

365   In spring, DOC transports behave in a similar way in all the water column. At SW and CW levels, $-2.33 \pm 0.57 \times 10^8 \, \mathrm{mol\,C\,day^{-1}}$ enter through the northern transect, of which $0.89 \pm 0.25 \times 10^8 \, \mathrm{mol\,C\,day^{-1}}$ leave the box through the southern transect and approximately a half of it through the western transect. During fall, there is an important outward DOC transport at SW, CW and IW levels, specially southward through the southern transect at SW and CW levels with a total of $1.48 \pm 0.66 \times 10^8 \, \mathrm{mol\,C\,day^{-1}}$ (Tab. 8).

370   Two opposite trends can be observed when both cruises are compared. In fall the IN net transports are -0.34 ± 0.20, -0.67 ± 0.40 and $-0.04 \pm 0.02 \, \mathrm{kmol\,s^{-1}}$ at CW levels; -0.17 ± 1.07, -0.23 ± 1.39 and $-0.01 \pm 0.09 \, \mathrm{kmol\,s^{-1}}$ at IW levels, and -0.12 ± 0.25, -0.10 ± 0.21 and $-0.01 \pm 0.01 \, \mathrm{kmol\,s^{-1}}$ at DW levels. The amount of nutrients entering the box is larger than those leaving the box with the exception at the shallowest level where the IN leave the box (Tabs. 5, 6 and 7 and Figs. 15 and 16). On the other hand, the net DOC transports are outward for both SW, CW and IW levels with $0.10 \pm 0.13 \times 10^8 \, \mathrm{mol\,C\,day^{-1}}$

375   at SW level, $1.34 \pm 0.80 \times 10^8 \, \mathrm{mol\,C\,day^{-1}}$ at CW levels, and $0.12 \pm 0.72 \times 10^8 \, \mathrm{mol\,C\,day^{-1}}$ at IW (Tab. 8 and Fig. 16).

In contrast, during spring a net outward transport is obtained for the three IN with 0.28 ± 0.61, 0.57 ± 1.22 and $0.04 \pm 0.08 \, \mathrm{kmol\,s^{-1}}$ at CW, 0.28 ± 0.72, 0.36 ± 0.94 and $0.02 \pm 0.06 \, \mathrm{kmol\,s^{-1}}$ at IW, and 0.13 ± 6.79, 0.12 ± 6.26 and $0.01 \pm 0.42 \, \mathrm{kmol\,s^{-1}}$ at DW (Tabs. 5, 6 and 7, and Figs. 15 and 16). On the other hand, the DOC net transports are inward with $-0.14 \pm 0.08 \times 10^8 \, \mathrm{mol\,C\,day^{-1}}$ at SW level; $-0.80 \pm 1.72 \times 10^8 \, \mathrm{mol\,C\,day^{-1}}$ at CW levels; and $-0.01 \pm 0.02 \times 10^8 \, \mathrm{mol\,C\,day^{-1}}$

380   at IW levels (Tab. 8 and Fig. 16).

6   DISCUSSION

The circulation patterns in the studied area of the Canary Basin change significantly showing a seasonal variability from fall to spring. The differences between the two seasons are reflected in the estimated mass transports for both cruises (Fig. 13 and Tab. 4).

Ocean Science
Discussions

385   Trade Winds are intense all year long between the Canary Islands and Cape Blanc (26° N to 21° N), and generate a quasi-permanent upwelling in this region north of Cape Blanc. In contrast, the developed EBUS intensity and its off-shore development change from fall to spring (Benazzouz et al., 2014). In the beginning of spring there is a strong heating that generates a sharp water stratification particularly in the interior ocean of the NASG and a very intense upwelling which makes the EBUS to develop strongly far off-shore. In early fall, the EBUS weakens and becomes a shallower front which approaches towards

390   the coast (Pelegrí and Benazzouz, 2015a). In fact, the variability related to its location and intensity may be the cause that the estimated mass transports in the north-south direction are distributed between levels of central waters and intermediate waters in fall, and that in spring these mass transports parallel to the coast are confined to the shallowest layers at central waters. On the other hand, these changes in the EBUS and in the water stratification may also be related to the westward mass transports which in fall are accentuated and confined to the levels of SW and CW, as a shallow Ekman transport, while in spring the

395   lateral westward transport is distributed from the sea surface down to IW levels (Tab. 4 and Fig. 13).

       SW transports through the N and W transects show similar patterns but in fall they are significantly more intense than in spring. In addition, CW level transports through these two transects show also similar patterns with a low variability between both seasons. The largest differences are observed in the estimated transports through the S transect which changes from fall to spring, where the transport is northward during fall and southward during spring. This observed variability in the transports in

400   SW and CW levels in the southern part of the domain is likely related to the seasonal changes in the position of CVFZ which in turn is related to the seasonal changes in the North Atlantic Tropical Gyre (NATG), south of the domain (Pelegrí et al., 2017). The fact that the Intertropical Convergence Zone moves southward in winter and northward in summer affects the circulation patterns south and north of Cape Blanc (Lázaro et al., 2005; Stramma et al., 2008; Peña-Izquierdo et al., 2012). While in fall the CVFZ crosses the S transect in its westernmost position, in spring it moves closer to the African coast. The output of the

405   GLORYS model matches the observations during both seasons (Fig. 14). In addition, the dynamics described by the geostrophic field of GLORYS also agree with the velocity field and the mass transports at CW levels estimated by the inverse model in the S transect for both seasons.

       GLORYS velocity outputs also reproduces the meso and submesocale associated with the CVFZ (Pérez-Rodríguez et al., 2001; Martínez-Marrero et al., 2008) which are observed directly in the S transect of the velocity sections (Fig. 10) and in the

410   accumulative mass transport (black line in Fig. 13). Specifically during fall, the reported eddies boost a significant transport at SW and CW levels from south to north. All these results at CW levels are consistent with the late-summer and fall growth of the Mauritania Current and of the PUC and also with the decrease of the NATG currents and the weakening of the Guinea Dome in winter and spring seasons (Siedler et al., 1992; Lázaro et al., 2005; Peña-Izquierdo et al., 2012; Pelegrí and Peña-Izquierdo, 2015; Pelegrí and Benazzouz, 2015a). The estimated transports at IW also show seasonal changes between fall and spring. This

415   region is featured by a late summer northward progression of AAIW observed in fall, and by a weak southward flow of MW in spring (Machín et al., 2010).

       In general, the estimated transports of the three IN show similar patterns, very marked by the mass transport variability during both seasons. The level with the highest transport in all the nutrients at both seasons is the deepest CW layer.

This is quite in agreement with the local maximum of remineralization found for all tracers in the upper intermediate layer
420   Fernández-Castro et al. (2018).

CW levels are featured by a relatively high biological production and therefore a nutrient deficit, and also by large geostrophic velocities. During fall the amount of IN that enters the box through N and S transects is larger than the IN quantity that leaves the box through the W transect. In spring, on the other hand, the amount of IN transported outward through the W and S transects is larger than the IN which enters from the north.

425   At IW levels the concentrations of IN are high and stable related to the dominant remineralization process. During spring, the spatial distribution of the three IN transports are the same as at CW levels with smaller values. In this season the transports of IN are directed westward through the W transect towards the oligotrophic open ocean. In fall, the IN transports at IW levels have a behaviour different than at CW levels being the main transport in the south-north direction.

The most significant differences between the DOC transports in fall and spring are obtained in the first and second shallowest
430   layers where there are high lateral velocities and where the euphotic layer is located. During fall, the DOC quantity that enters by the north transect is a third of the amount that leaves the region by the south. In the spring, however, the large amount of DOC that enters the domain from the north doubles the quantity that leaves it by the S transect while a quarter does by the western transect.

In spring, when the stratification is less marked, the most significant and deepest transports of IN are observed toward
435   the open ocean in central and intermediate water levels. However, in fall, when the water column is more stratified and the upwelling process is the main physical forcing for nutrient supply at CW levels (Pastor et al., 2013), the IN transports toward oligotrophic interior ocean is less than in spring. In fact, while in the western transect during spring the IN transports increase with depth to their maximum values at the deepest central layer, in fall the opposite occurs, since the westward IN transports decrease with depth until cancelling at the last central layer; these transports reverse towards the coast at the two intermediate
440   layers (green line in Figs. 15 and 16).

On the other hand, DOC transports are deeper and more intensified toward the open ocean during spring than in fall. Nonetheless, in fall there is an important and deeper transport of IN in a direction parallel to the coast. In fact, at IW DOC concentrations accumulate next to the African coast in the upwelling region. Furthermore, inside the upwelling region at the N and S transects in fall, the two observed mesoscale anticyclonic eddies could accentuate this process.

445   The variability in intensity of the stratification, strength of upwelling and the position of the boundary between the upwelling and the oligotrophic interior ocean together with important meso and submesocale structures control the nutrients availability at CW and IW waters. It is also deduced from DOC transport estimates that the upwelling drives the changes in the size of the high production domain and equivalently, the position for the eastern boundary of the oligotrophic region in this area (Pastor et al., 2013).

450   The estimated transports of IN and DOC tell us that in fall there is a pronounced import of IN into the domain (with the exception of the SW layer) and a moderate export of DOC, especially at CW and IW levels. On the other hand, during spring there is a pronounced export of IN from the domain at CW and IW levels and a slight import of DOC at the shallowest CW levels and at the SW layer.

7 CONCLUSIONS

In summary, the net mass transports across the 3 transects are shown in Figure 17 for the different water layers and for both seasons. In this figure, the main changes of the net mass transports from fall to spring are observed. The net mass transport at CW layers coincides in both seasons in the N transect with a southward flow of -2.94 ± 1.26 Sv in fall that increases in spring to -4.89 ± 1.14 Sv. In the W transect the net westward mass transport at CW levels weakens from a value of 3.50 ± 1.09 Sv in fall to 2.96 ± 1.06 Sv in spring. The most remarkable change in the net mass transport at CW layers occurs in the southern transect where in fall the net mass transport is northward with a value of -3.85 ± 1.03 Sv, while in spring it is southward with a value of 2.80 ± 1.02 Sv. In the shallowest layer, the SW transports follow a pattern similar to those at CW levels across the 3 transects. However, in fall higher SW transports through the N and W transects are obtained, -2.67 ± 0.60 and 2.46 ± 0.66 Sv, respectively, and in spring there is a higher SW transport through the S transect with 2.40 ± 0.53 Sv.

At IW layers, the net transport in the south-north direction is intense and northward in fall, 1.94 ± 1.85 Sv, while it weakens and reverses southward in spring, -0.48 ± 1.65 Sv. In the W transect, the net westward mass transport at IW layers is less intense in fall, 0.48 ± 1.71 Sv, than in spring, 1.21 ± 1.68 Sv. Last, the net mass transport at DW levels is small as compared to the other water levels, with the exception of the 0.73 ± 1.71 Sv estimated in the N transect during fall.

From a physical perspective, it has been analysed how these transports influence the transports of IN and DOC in the study area. It has also been observed how other non-physical factors determine the distribution of IN and DOC in the area of interest due to their link within the biogeochemical cycles. It is noted how in fall, the domain works as a nutrient sink with total IN net import of -0.61 ± 1.97, -0.74 ± 2.40 and -0.05 ± 0.15 $\mathrm{kmol\,s^{-1}}$ of SiO_2, NO_3 and PO_4, respectively, and how in spring it works as a source of nutrients with a total nutrient net export of 0.73 ± 0.91, 1.21 ± 1.51 and 0.08 ± 0.1 $\mathrm{kmol\,s^{-1}}$. And it is also observed how the net DOC outward transport is of $1.55 \pm 5.01 \times 10^8 \mathrm{\,mol\,C\,day^{-1}}$ in fall makes the domain act as a source of DOC in this season and how the significant negative value of $-0.95 \pm 1.19 \times 10^8 \mathrm{\,mol\,C\,day^{-1}}$ describes it as a DOC sink in spring.

However, what is really interesting here is to analyse the lateral transports of both IN and DOC towards the oligotrophic ocean and their seasonal variability. During spring there is a continuous westward IN transport, 0.75 ± 0.37, 1.34 ± 0.66 and 0.08 ± 0.04 $\mathrm{kmol\,s^{-1}}$ of SiO_2, NO_3 and PO_4, respectively, toward the open ocean through the W transect in all the water column that coincide with an important transport of DOC, $0.50 \pm 0.25 \times 10^8 \mathrm{\,mol\,C\,day^{-1}}$, mainly at SW and CW. In fall, these transports are weakened at CW and reverse at IW, which means that the net westward transport of IN is smaller than in spring, with values of 0.03 ± 0.01, 0.35 ± 0.13 and 0.02 ± 0.01 $\mathrm{kmol\,s^{-1}}$ for SiO_2, NO_3 and PO_4 towards oligotrophic waters. Westward transport of DOC is not observed even at the shallowest layer.

It is still necessary to continue with the understanding of the physical and biogeochemical processes and the interactions between the productive EBUS and the interior ocean in its vicinity, especially in dynamically complex regions as this area where the EBUS interacts with the CVFZ. Larger and more robust hydrological and biogeochemical databases would help to achieve this goal.

Ocean Science
Discussions

Acknowledgements. This work has been done thanks to the project COCA (REN2000-U471-CO2-02-MAR) and it was supported by the project FLUXES (CTM2015-69392-C3-3-R), both of them funded by the Spanish National Research Program. Currently, NB is working on her Ph.D. with a fellowship funded by the Spanish Ministry of Economy and Competitiveness.

References

490 Alonso-González, I. J., Arístegui, J., Vilas, J. C., and Hernández-Guerra, A.: Lateral POC transport and consumption in surface and deep waters of the Canary Current region: A box model study, Global Biogeochemical Cycles, 23, 1–12, https://doi.org/10.1029/2008GB003185, 2009.

Álvarez, M. and Álvarez-Salgado, X. A.: Chemical tracer transport in the eastern boundary current system of the North Atlantic, Ciencias

495 Marinas, 35, 123–139, 2009.

Álvarez-Salgado, X. A., Arístegui, J., Barton, E. D., and Hansell, D. A.: Contribution of upwelling filaments to offshore carbon export in the subtropical Northeast Atlantic Ocean, Limnology and Oceanography, 52, 1287–1292, https://doi.org/10.4319/lo.2007.52.3.1287, 2007.

Arístegui, J., Sangrá, P., Hernández-León, S., Cantón, M., Hernández-Guerra, A., and Kerling, J.: Island-induced eddies in the Canary Islands, Deep Sea Research Part I: Oceanographic Research Papers, 41, 1509–1525, 1994.

500 Arístegui, J., Barton, E. D., Álvarez-Salgado, X. A., Santos, A. M. P., Figueiras, F. G., Kifani, S., Hernández-León, S., Mason, E., Machú, E., and Demarcq, H.: Sub-regional ecosystem variability in the Canary Current upwelling, Progress in Oceanography, 83, 33–48, 2009.

Azam, F.: Microbial control of oceanic carbon flux: the plot thickens, Science, 280, 694–696, 1998.

Barceló-Llull, B., Sangrà, P., Pallàs-Sanz, E., Barton, E. D., Estrada-Allis, S. N., Martínez-Marrero, A., Aguiar-González, B., Grisolía, D., Gordo, C., Rodríguez-Santana, Á., et al.: Anatomy of a subtropical intrathermocline eddy, Deep Sea Research Part I: Oceanographic

505 Research Papers, 124, 126–139, 2017a.

Barceló-Llull, B., Pallàs-Sanz, E., Sangrà, P., Martínez-Marrero, A., Estrada-Allis, S. N., and Arístegui, J.: Ageostrophic Secondary Circulation in a Subtropical Intrathermocline Eddy, Journal of Physical Oceanography, 47, 1107–1123, https://doi.org/10.1175/JPO-D-16-0235.1, http://journals.ametsoc.org/doi/10.1175/JPO-D-16-0235.1, 2017b.

Barton, E.: The poleward undercurrent on the eastern boundary of the subtropical North Atlantic, Springer, 1989.

510 Barton, E. D., Arístegui, J., Tett, P., Canton, M., García-Braun, J., Hernández-León, S., Nykjaer, L., Almeida, C., Almunia, J., Ballesteros, S., Basterretxea, G., Escanez, J., García-Weill, L., Hernández-Guerra, A., López-Laatzen, F., Molina, R., Montero, M. F., Navarro-Peréz, E., Rodríguez, J. M., Van Lenning, K., Vélez, H., and Wild, K.: The transition zone of the Canary Current upwelling region, Progress in Oceanography, 41, 455–504, https://doi.org/10.1016/S0079-6611(98)00023-8, 1998.

Benazzouz, A., Pelegrí, J. L., Demarcq, H., Machín, F., Mason, E., Orbi, A., Peña-Izquierdo, J., and Soumia, M.: On the temporal memory of

515 coastal upwelling off NW Africa, Journal of Geophysical Research C: Oceans, 119, 6356–6380, https://doi.org/10.1002/2013JC009559, 2014.

Candela, J.: Chapter 5.7 Mediterranean water and global circulation, in: International Geophysics, vol. 77, pp. 419–429, Elsevier, 2001.

Comas-Rodríguez, I., Hernández-Guerra, A., Fraile-Nuez, E., Martínez-Marrero, A., Benítez-Barrios, V. M., Pérez-Hernández, M., and Vélez-Belchí, P.: The Azores Current System from a meridional section at 24.5 W, Journal of Geophysical Research: Oceans, 116, 2011.

520 Copin-Montegut, C. and Copin-Montegut, G.: Stoichiometry of carbon, nitrogen, and phosphorus in marine particulate matter, Deep Sea Research Part A. Oceanographic Research Papers, 30, 31–46, 1983.

Del Giorgio, P. A. and Duarte, C. M.: Respiration in the open ocean, Nature, 420, 379, 2002.

Ekman, V. W.: Über Horizontalzirkulation bei winderzeugten Meeresströmungen, R. Friedländer & Sohn, 1923.

Emery, W. J.: Water Types and Water Masses, Encyclopedia of Ocean Sciences: Second Edition, pp. 291–299,

525 https://doi.org/10.1016/B978-012374473-9.00108-9, 2008.

Emery, W. J. and Meincke, J.: Global water masses: summary and review, Oceanologica Acta, 9, 383–391, 1986.

Estrada-Allis, S., Barceló-Llull, B., Pallàs-Sanz, E., Rodríguez-Santana, A., Souza, J., Mason, E., McWilliams, J., and Sangrà, P.: Vertical Velocity Dynamics and Mixing in an Anticyclone near the Canary Islands, Journal of Physical Oceanography, 49, 431–451, 2019.

Falkowski, P. G., Barber, R. T., and Smetacek, V.: Biogeochemical controls and feedbacks on ocean primary production, Science, 281, 530   200–206, 1998.

Fernández-Castro, B., Mouriño-Carballido, B., and Álvarez-Salgado, X. A.: Non-redfieldian mesopelagic nutrient remineralization in the eastern North Atlantic subtropical gyre, Progress in Oceanography, 171, 136–153, 2018.

Fiekas, V., Elken, J., Muller, T. J., Aitsam, A., and Zenk, W.: A view of the Canary Basin thermocline circulation in winter, Journal of Geophysical Research, 97, 12 495–12 510, https://doi.org/10.1029/92JC01095, 1992.

535 Fu, Y., Karstensen, J., and Brandt, P.: Atlantic Meridional Overturning Circulation at 14.5° N in 1989 and 2013 and 24.5° N in 1992 and 2015: volume, heat, and freshwater transports, Ocean Science, 14, 589–616, https://doi.org/10.5194/os-14-589-2018, https://www.ocean-sci.net/14/589/2018/, 2018.

Ganachaud, A.: Large-scale mass transports, water mass formation, and diffusivities estimated from World Ocean Circulation Experiment (WOCE) hydrographic data, Journal of Geophysical Research, 108, 3213, https://doi.org/10.1029/2002JC001565, 540   http://doi.wiley.com/10.1029/2002JC001565, 2003a.

Ganachaud, A.: Error budget of inverse box models: The North Atlantic, Journal of Atmospheric and Oceanic Technology, 20, 1641–1655, 2003b.

Ganachaud, A. and Wunsch, C.: Large-scale ocean heat and freshwater transports during the world ocean circulation experiment, Journal of Climate, 16, 696–705, 2002a.

545 Ganachaud, A. and Wunsch, C.: Oceanic nutrient and oxygen transports and bounds on export production during the World Ocean Circulation Experiment, Global Biogeochemical Cycles, 16, 5–1, 2002b.

Ganachaud, A. S.: Large Scale Oceanic Circulation and Fluxes of Freshwater, Heat, Nutrients and Oxygen, Ph.D. thesis, Massachusetts Institute of Technology and Woods Hole Oceanographic Institution, https://doi.org/10.1575/1912/4130, 1999.

García-Muñoz, M., Arístegui, J., Montero, M. F., and Barton, E. D.: Distribution and transport of organic matter along a 550   filament-eddy system in the Canaries - NW Africa coastal transition zone region, Progress in Oceanography, 62, 115–129, https://doi.org/10.1016/j.pocean.2004.07.005, 2004.

Hagen, E.: Northwest African upwelling scenario, Oceanologica Acta, 24, 113–128, https://doi.org/10.1016/S0399-1784(00)01110-5, 2001.

Halkin, D., Rossby, H. T., and Rossby, T.: Structure and Transport of the Gulf Stream at 73 N, JPhysOceanogr, 15, 1439–1452, 1985.

Hansell, D. A.: DOC in the global ocean carbon cycle, Biogeochemistry of marine dissolved organic matter, 2002.

555 Hansen, H. P. and Koroleff, F.: Determination of nutrients, Chapter 10, Methods of Seawater Analysis, Wiley-VCH Verlag GmbH, https://doi.org/10.1002/9783527613984, 1999.

Haynes, R., Barton, E. D., and Pilling, I.: Development, persistence, and variability of upwelling filaments off the Atlantic coast of the Iberian Peninsula, Journal of Geophysical Research, 98, 22 681, https://doi.org/10.1029/93JC02016, http://doi.wiley.com/10.1029/93JC02016, 1993.

560 Hempel, G.: The Canary Current:Studies of an Upwelling System, A Symposium held in Las Palmas, 11-14 April 1978, Secretariat of the International Council for the Exploration of the Sea, 180, 1982.

Hernández-Guerra, A., Arístegui, J., Cantón, M., and Nykjaer, L.: Phytoplankton pigment patterns in the Canary Islands area as determined using Coastal Zone Colour Scanner data, International Journal of Remote Sensing, 14, 1431–1437, 1993.

Hernández-Guerra, A., Fraile-Nuez, E., López-Laatzen, F., Martínez, A., Parrilla, G., and Vélez-Belchí, P.: Canary Current and North Equa-
565   torial Current from an inverse box model, Journal of Geophysical Research: Oceans, 110, 1–16, https://doi.org/10.1029/2005JC003032,
2005.

Hernández-Guerra, A., Espino-Falcón, E., Vélez-Belchí, P., Pérez-Hernández, M. D., Martínez-Marrero, A., and Cana, L.: Recirculation of
the Canary Current in fall 2014, Journal of Marine Systems, 174, 25–39, https://doi.org/10.1016/j.jmarsys.2017.04.002, 2017.

Hernández-León, S., Putzeys, S., Almeida, C., Bécognée, P., Marrero-Díaz, A., Arístegui, J., and Yebra, L.: Carbon export through zoo-
570   plankton active flux in the Canary Current, Journal of Marine Systems, 189, 12–21, https://doi.org/10.1016/j.jmarsys.2018.09.002,
https://doi.org/10.1016/j.jmarsys.2018.09.002, 2019.

Hughes, P. and Barton, E. D.: Stratification and water mass structure in the upwelling area off northwest Africa in April/May 1969, Deep-Sea
Research and Oceanographic Abstracts, 21, https://doi.org/10.1016/0011-7471(74)90046-1, 1974.

Jackett, D. R. and McDougall, T. J.: A Neutral Density Variable for the World's Oceans, Journal of Physical Oceanography, 27, 237–263,
575   1997.

Käse, R., Price, J., Richardson, P., and Zenk, W.: A Quasi-Synoptic Survey of the Thermocline Circulation and Water Mass Distribution
Within the Canary Basin, Journal of Geophysical Research: Oceans, 91, 9739–9748, 1986.

Käse, R. H. and Siedler, G.: Meandering of the subtropical front south-east of the Azores, Nature, 300, 245–246, 1982.

Lázaro, C., Fernandes, M. J., Santos, A. M. P., and Oliveira, P.: Seasonal and interannual variability of surface circulation in
580   the Cape Verde region from 8 years of merged T/P and ERS-2 altimeter data, Remote Sensing of Environment, 98, 45–62,
https://doi.org/10.1016/j.rse.2005.06.005, 2005.

Luyten, J., Pedlosky, J., and Stommel, H.: The ventilated thermocline, Journal of Physical Oceanography, 13, 292–309, 1983.

Macdonald, A. M.: The global ocean circulation: A hydrographic estimate and regional analysis, Progress in Oceanography, 41, 281–382,
https://doi.org/10.1016/S0079-6611(98)00020-2, 1998.

585   Machín, F.: Variabilidad espacio temporal de la Corriente de Canarias, del afloramiento costero al noroeste de África y de los intercambios
atmósfera-océano de calor y agua dulce, Ph.D. thesis, Universidad de Las Palmas de Gran Canaria, 2003.

Machín, F. and Pelegrí, J. L.: Northward penetration of Antarctic intermediate water off Northwest Africa, Journal of Physical Oceanography,
39, 512–535, 2009.

Machín, F., Hernández-Guerra, A., and Pelegrí, J. L.: Mass fluxes in the Canary Basin, Progress in Oceanography, 70, 416–447,
590   https://doi.org/10.1016/j.pocean.2006.03.019, 2006.

Machín, F., Pelegrí, J. L., Fraile-Nuez, E., Vélez-Belchí, P., López-Laatzen, F., and Hernández-Guerra, A.: Seasonal Flow Reversals of
Intermediate Waters in the Canary Current System East of the Canary Islands, Journal of Physical Oceanography, 40, 1902–1909,
https://doi.org/10.1175/2010JPO4320.1, http://journals.ametsoc.org/doi/abs/10.1175/2010JPO4320.1, 2010.

Martel, F. and Wunsch, C.: The North Atlantic Circulation in the Early 1980s-An Estimate from Inversion of a Finite-Difference Model,
595   Journal of Physical Oceanography, 23, 898–924, 1993.

Martínez-Marrero, A., Rodríguez-Santana, A., Hernández-Guerra, A., Fraile-Nuez, E., López-Laatzen, F., Vélez-Belchí, P., and Parrilla,
G.: Distribution of water masses and diapycnal mixing in the Cape Verde Frontal Zone, Geophysical Research Letters, 35, 0–4,
https://doi.org/10.1029/2008GL033229, 2008.

MATLAB: version R2018b, The MathWorks Inc., Natick, Massachusetts, https://www.mathworks.com/products/matlab.html, 2018.

600   Mittelstaedt, E.: The upwelling area off Northwest Africa—A description of phenomena related to coastal upwelling, Progress in Oceanog-
raphy, 12, 307–331, 1983.

Mittelstaedt, E.: The ocean boundary along the northwest African coast: Circulation and oceanographic properties at the sea surface, Progress in Oceanography, 26, 307–355, https://doi.org/https://doi.org/10.1016/0079-6611(91)90011-A, 1991.

Paillet, J. and Mercier, H.: An inverse model of the eastern North Atlantic general circulation and thermocline ventilation, Deep-Sea Research Part I: Oceanographic Research Papers, 44, 1293–1328, https://doi.org/10.1016/S0967-0637(97)00019-8, 1997.

Pastor, M. V., Pelegrí, J. L., Hernández-Guerra, A., Font, J., Salat, J., and Emelianov, M.: Water and nutrient fluxes off Northwest Africa, Continental Shelf Research, 28, 915–936, 2008.

Pastor, M. V., Palter, J. B., Pelegrí, J. L., and Dunne, J. P.: Physical drivers of interannual chlorophyll variability in the eastern subtropical North Atlantic, Journal of Geophysical Research: Oceans, 118, 3871–3886, https://doi.org/10.1002/jgrc.20254, 2013.

Pelegrí, J. L. and Benazzouz, A.: Oceanographic and biological features in the Canary Current Large Marine Ecosystem, Chapter 3.4, Coastal Upwelling off north-west Africa, IOC Technical Series, 115, 2015a.

Pelegrí, J. L. and Benazzouz, A.: Oceanographic and biological features in the Canary Current Large Marine Ecosystem, Chapter 4.1, Inorganic nutrients and dissolved oxygen in the Canary Current large marine ecosystem, IOC Technical Series, 115, 2015b.

Pelegrí, J. L. and Peña-Izquierdo, J.: Oceanographic and biological features in the Canary Current Large Marine Ecosystem, Chapter 3.3, Eastern Boundary currents off north-west Africa, IOC Technical Series, 115, 2015.

Pelegrí, J. L., Arístegui, J., Cana, L., González-Dávila, M., Hernández-Guerra, A., Hernández-León, S., Marrero-Díaz, A., Montero, M. F., Sangrà, P., and Santana-Casiano, M.: Coupling between the open ocean and the coastal upwelling region off northwest Africa: Water recirculation and offshore pumping of organic matter, Journal of Marine Systems, 54, 3–37, https://doi.org/10.1016/j.jmarsys.2004.07.003, 2005.

Pelegrí, J. L., Marrero-Díaz, A., and Ratsimandresy, A. W.: Nutrient irrigation of the North Atlantic, Progress in Oceanography, 70, 366–406, https://doi.org/10.1016/j.pocean.2006.03.018, 2006.

Pelegrí, J. L., Peña-Izquierdo, J., Machín, F., Meiners, C., and Presas-Navarro, C.: Deep-Sea Ecosystems Off Mauritania, Chapter 3, Oceanography of the Cape Verde Basin and Mauritanian Slope Waters, Springer, 2017.

Peña-Izquierdo, J., Pelegrí, J. L., Pastor, M. V., Castellanos, P., Emelianov, M., Gasser, M., Salvador, J., and Vázquez-Domínguez, E.: The continental slope current system between Cape Verde and the Canary Islands, Scientia Marina, 76, 65–78, https://doi.org/10.3989/scimar.03607.18C, 2012.

Pérez, F. F., Mintrop, L., Llinás, O., Glez-Dávila, M., Castro, C. G., Alvarez, M., Körtzinger, A., Santana-Casiano, M., Rueda, M. J., and Ríos, A. F.: Mixing analysis of nutrients, oxygen and inorganic carbon in the Canary Islands region, Journal of Marine Systems, 28, 183–201, https://doi.org/10.1016/S0924-7963(01)00003-3, 2001.

Pérez-Hernández, M. D., Hernández-Guerra, A., Fraile-Nuez, E., Comas-Rodríguez, I., Benítez-Barrios, V. M., Domínguez-Yanes, J. F., Vélez-Belchí, P., and De Armas, D.: The source of the Canary current in fall 2009, Journal of Geophysical Research: Oceans, 118, 2874–2891, https://doi.org/10.1002/jgrc.20227, 2013.

Pérez-Rodríguez, P., Pelegrí, J. L., and Marrero-Díaz, A.: Dynamical characteristics of the Cape Verde frontal zone, Scientia Marina, 65, 241–250, https://doi.org/10.3989/scimar.2001.65s1241, 2001.

Ruiz, S., Pelegrí, J., Emelianov, M., Pascual, A., and Mason, E.: Geostrophic and ageostrophic circulation of a shallow anticyclonic eddy off Cape Bojador, Journal of Geophysical Research: Oceans, 119, 1257–1270, 2014.

Sangrà, P., Auladell, M., Marrero-Díaz, A., Pelegrí, J. L., Fraile-Nuez, E., Rodríguez-Santana, A., Martín, J. M., Mason, E., and Hernández-Guerra, A.: On the nature of oceanic eddies shed by the Island of Gran Canaria, Deep-Sea Research Part I: Oceanographic Research Papers, 54, 687–709, https://doi.org/10.1016/j.dsr.2007.02.004, 2007.

640   Sangrà, P., Pascual, A., Rodríguez-Santana, Á., Machín, F., Mason, E., McWilliams, J. C., Pelegrí, J. L., Dong, C., Rubio, A., Arístegui,
      J., Marrero-Díaz, Á., Hernández-Guerra, A., Martínez-Marrero, A., and Auladell, M.: The Canary Eddy Corridor: A major pathway
      for long-lived eddies in the subtropical North Atlantic, Deep-Sea Research Part I: Oceanographic Research Papers, 56, 2100–2114,
      https://doi.org/10.1016/j.dsr.2009.08.008, 2009.

      Santana-Falcón, Y., Álvarez-Salgado, X. A., Pérez-Hernández, M. D., Hernández-Guerra, A., Mason, E., and Arístegui, J.: Organic carbon
645   budget for the eastern boundary of the North Atlantic subtropical gyre: Major role of DOC in mesopelagic respiration, Scientific Reports,
      7, 1–12, https://doi.org/10.1038/s41598-017-10974-y, 2017.

      Schlitzer, Reiner: Ocean Data View, http://odv.awi.de., 2019.

      Sharp, J., Peltzer, E., Alperin, M., Cauwet, G., Farrington, J., Fry, B., Karl, D., Martin, J., Spitzy, A., Tugrul, S., et al.: Procedures subgroup
      report, Marine Chemistry, 41, 37–49, 1993.

650   Siedler, G., Zangenberg, N., and Onken, R.: Seasonal Changes in the Tropical Atlantic Circulation: Observation and Simulation of the Guinea
      Dome, Journal of Geophysical Research, 97, 703–715, 1992.

      Smith, W. H. F. and Sandwell, D. T.: Global Sea Floor Topography from Satellite Altimetry and Ship Depth Soundings, Science, 277,
      1956–1962, https://doi.org/10.1126/science.277.5334.1956, http://science.sciencemag.org/content/277/5334/1956, 1997.

      Stramma, L.: Geostrophic transport in the warm water sphere of the eastern subtropical North Atlantic, Journal of Marine Research, 42,
655   537–558, https://doi.org/10.1357/002224084788506022, 1984.

      Stramma, L. and Siedler, G.: Seasonal changes in the North Atlantic subtropical gyre, Journal of Geophysical Research, 93, 8111,
      https://doi.org/10.1029/JC093iC07p08111, 1988.

      Stramma, L., Brandt, P., Schafstall, J., Schott, F., Fischer, J., and Körtzinger, A.: Oxygen minimum zone in the North Atlantic south and east
      of the Cape Verde Islands, Journal of Geophysical Research: Oceans, 113, 1–15, https://doi.org/10.1029/2007JC004369, 2008.

660   Thomas, C., Cauwet, G., and Minster, J.-F.: Dissolved organic carbon in the equatorial Atlantic Ocean, Marine Chemistry, 49, 155–169,
      1995.

      Tomczak, M.: The CINECA experience, Marine Policy, 3, 59–65, https://doi.org/https://doi.org/10.1016/0308-597X(79)90040-X, 1979.

      Tomczak, M. and Godfrey, J. S.: Regional oceanography, an introduction, Elsevier, 2nd edition edn., 2003.

      Wunsch, C.: North Atlantic general circulation west of 50°W determined by inverse methods, Reviews of Geophysics, 16, 583–620, 1978.

665   Wunsch, C.: The ocean circulation inverse problem, Cambridge University Press, Cambridge;New York;, 1996.

      Zenk, W., Klein, B., and Schroder, M.: Cape Verde Frontal Zone, Deep Sea Research Part A. Oceanographic Research Papers, 38, S505–
   S530, https://doi.org/10.1016/S0198-0149(12)80022-7, 1991.

Figures and tables
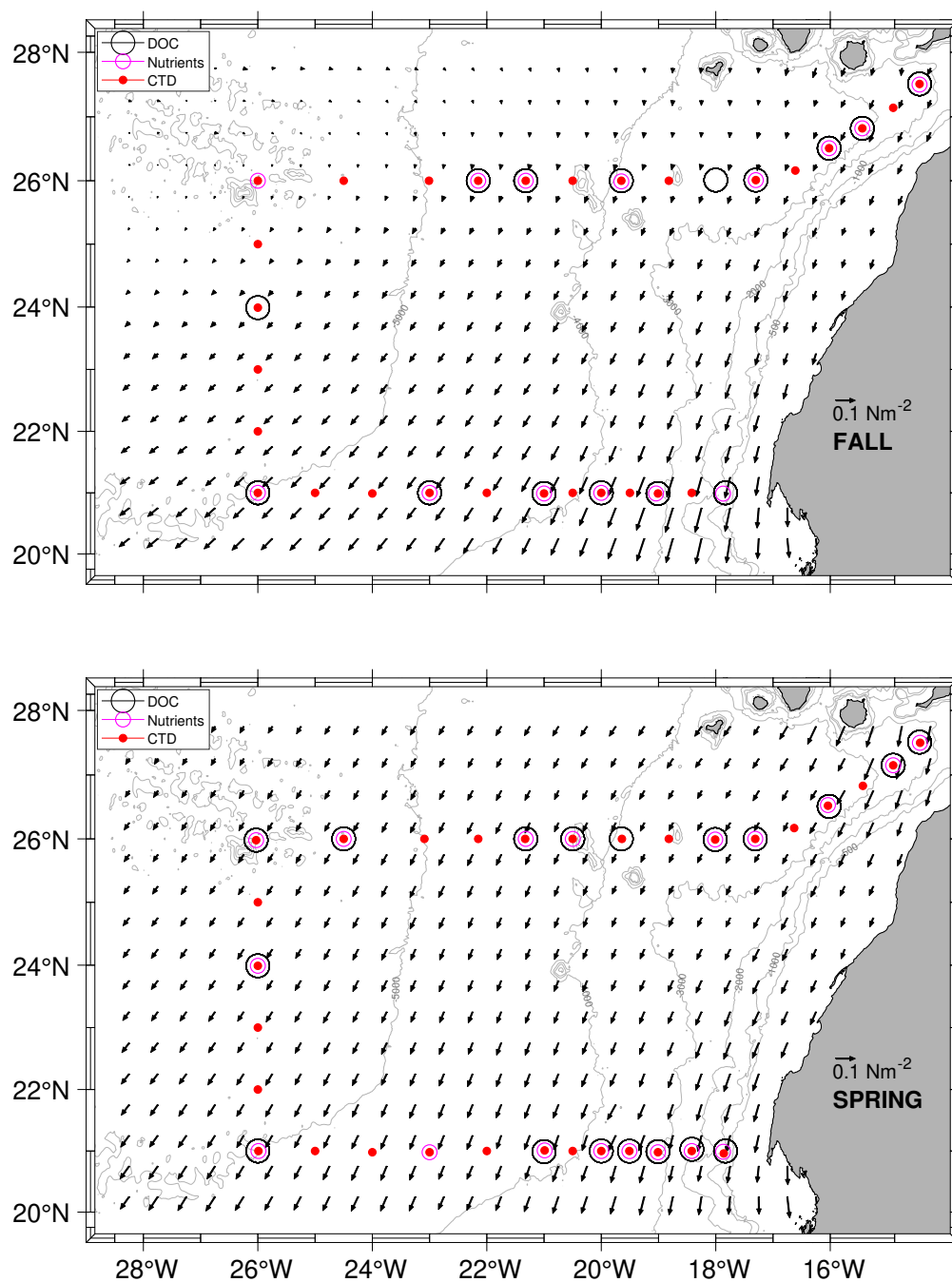
Figure 1. Hydrological (red dots), inorganic nutrients (pink circles) and DOC (black circles) sampling stations during cruises COCA-I (top) and COCA-II (bottom). Time-averaged wind stress during each cruise is also represented with the inset arrow denoting the scale (shown with half of the original spatial resolution).
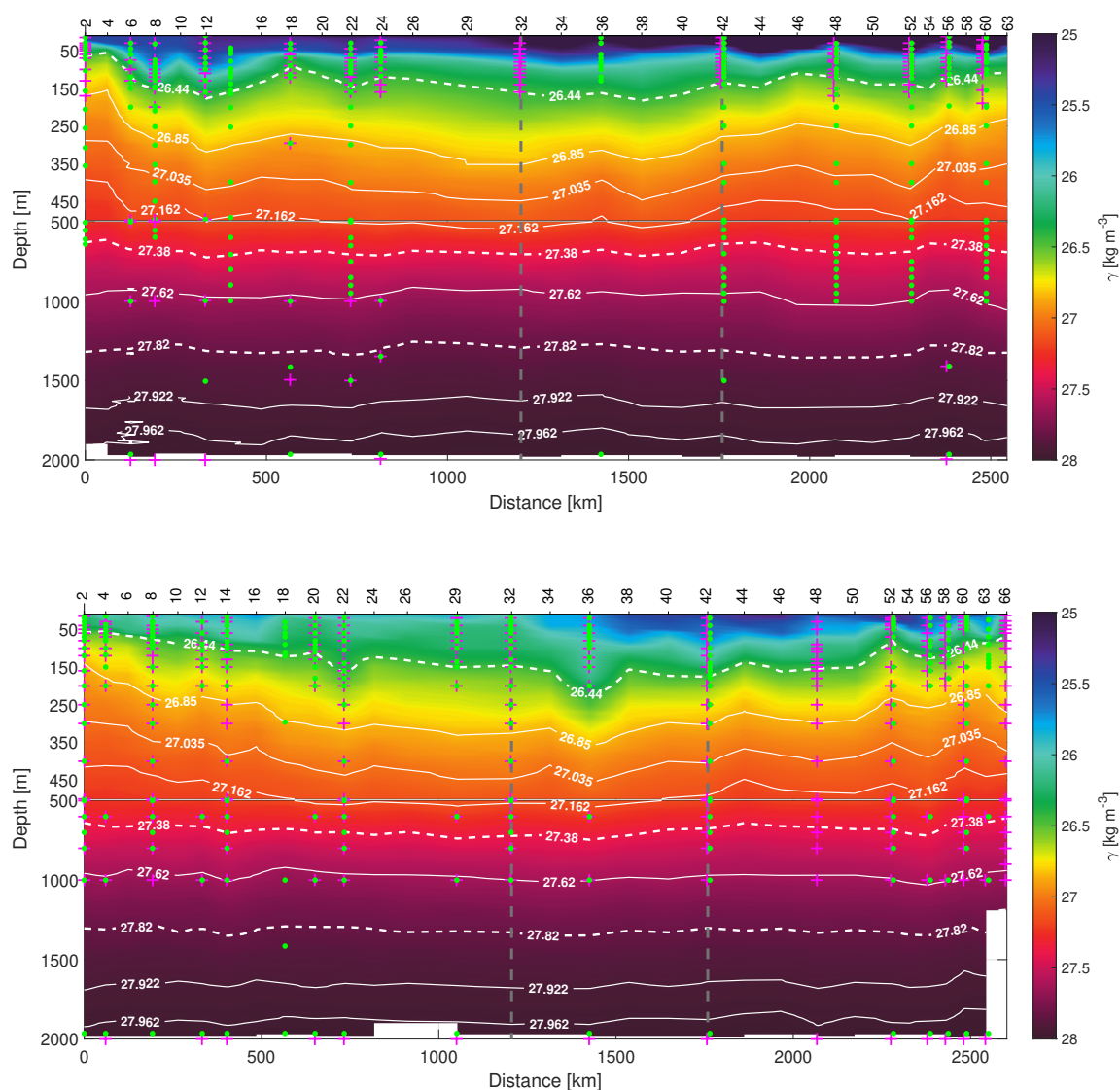
Figure 2. γ_n vertical sections during fall (top) and spring (bottom) cruises. White dashed isoneutrals limit the different water type layers. The direction chosen for the representation of the transects is the course of the vessel. Distance is calculated with respect to the first station (2). The section is divided into three transects: northern transect from east to west (from station 2 to 32), western transect from north to south (from station 32 to 42) and southern transect from west to east (from stations 42 to 63/66). The 3 transects are separated by two vertical grey dashed lines located at stations number 32 and 42. The sampling points of IN and DOC used in this work are also represented in pink crosses and green dots, respectively.
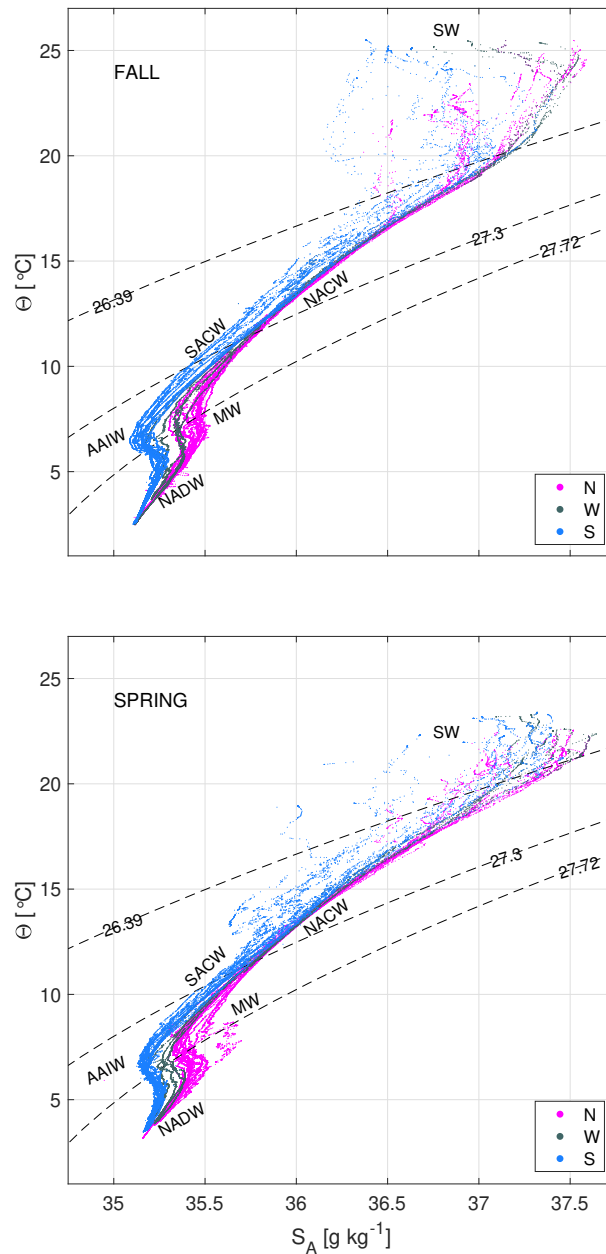
Figure 3. $\Theta - S_A$ diagrams of the hydrological measurements in fall (top) and spring (bottom) cruises. The different water masses at north (N, magenta dots), west (W, dark grey dots) and south (S, blue dots) transects are SW, NACW, SACW, AAIW, MW and NADW. Potential density anomaly contours equivalent to 26.44, 27.38 and 27.82 kg m^{-3} isoneutrals delimit the surface, central, intermediate and deep water levels.
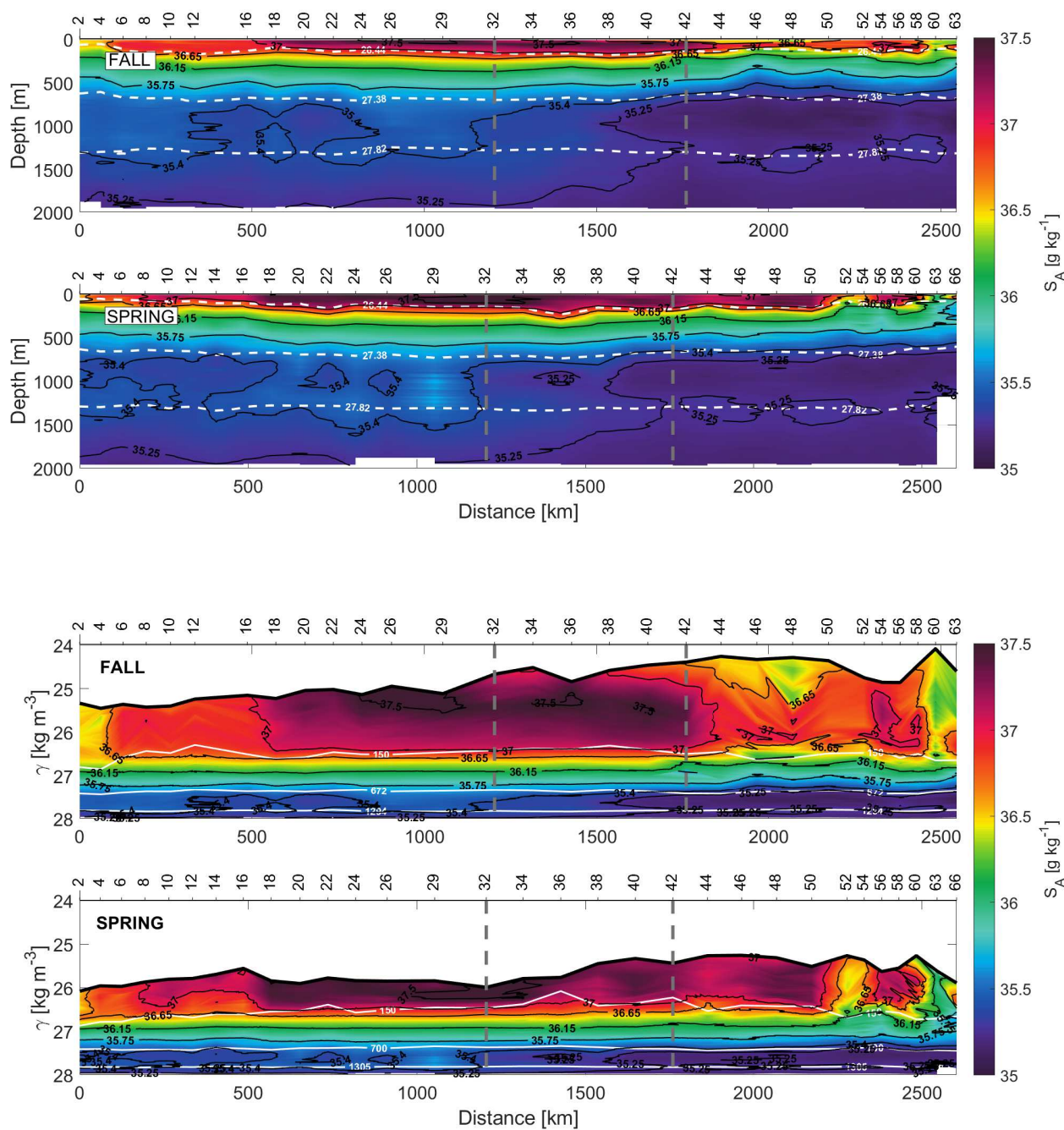
Figure 4. Sections of absolute salinity (S_A) with respect to depth (top) and γ_n (bottom) during fall and spring. In depth section (top), the isoneutrals which delimit the transports at surface, central, intermediate and deep water are represented by white dashed contours. In γ_n section (bottom), the depths of 150, 672/700 and 1204/1305 m are also shown.

Ocean Science
Discussions

Open Access

EGU
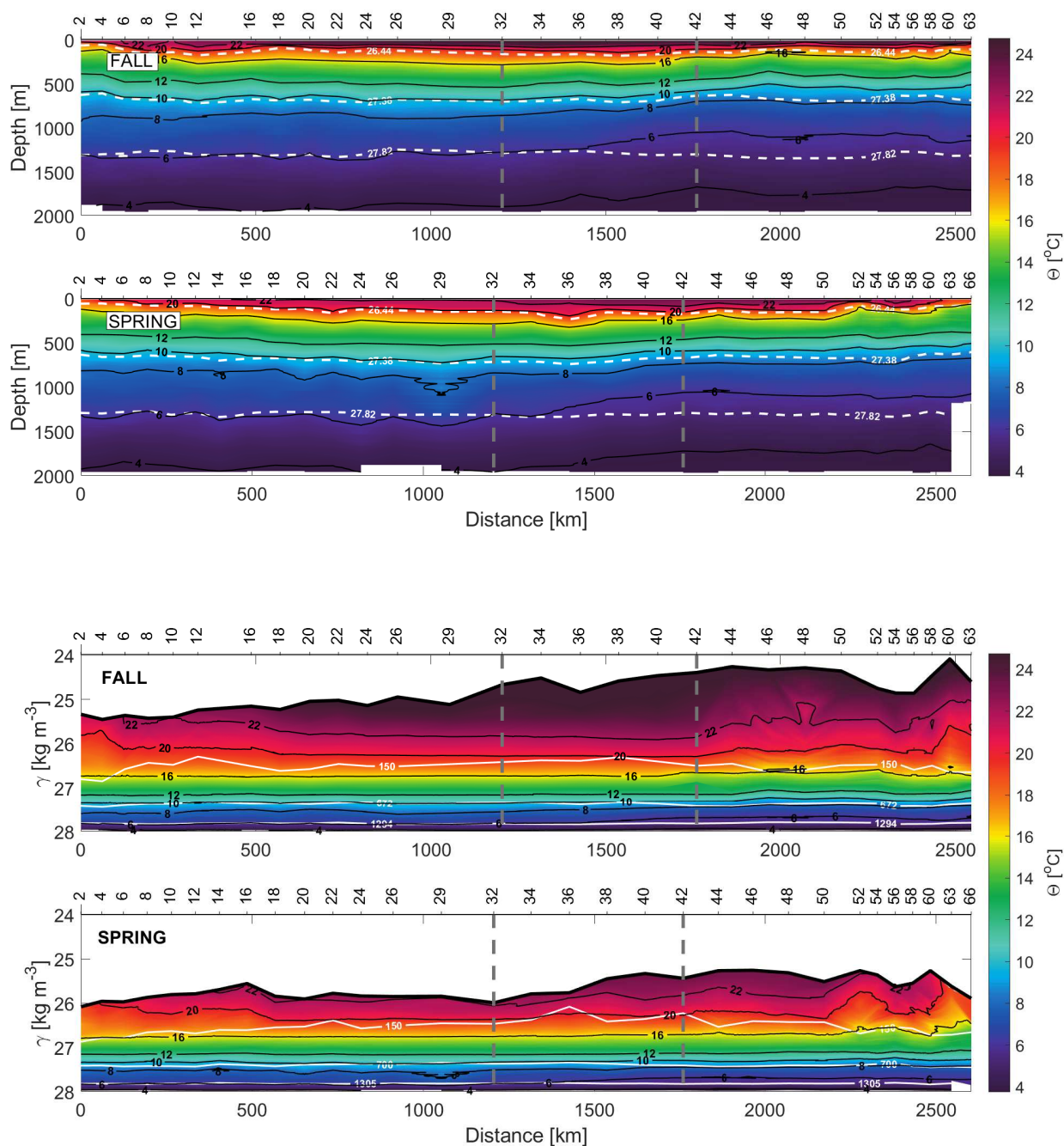
Figure 5. Sections of conservative temperature (Θ) with respect to depth (top) and γ_n (bottom) during fall and spring. In depth section (top), the isoneutrals which delimit the transports at surface, central, intermediate and deep water in the water column are represented by white dashed contours. In γ_n section (bottom), the depths of 150, 672/700 and 1204/1305 m are indicated.
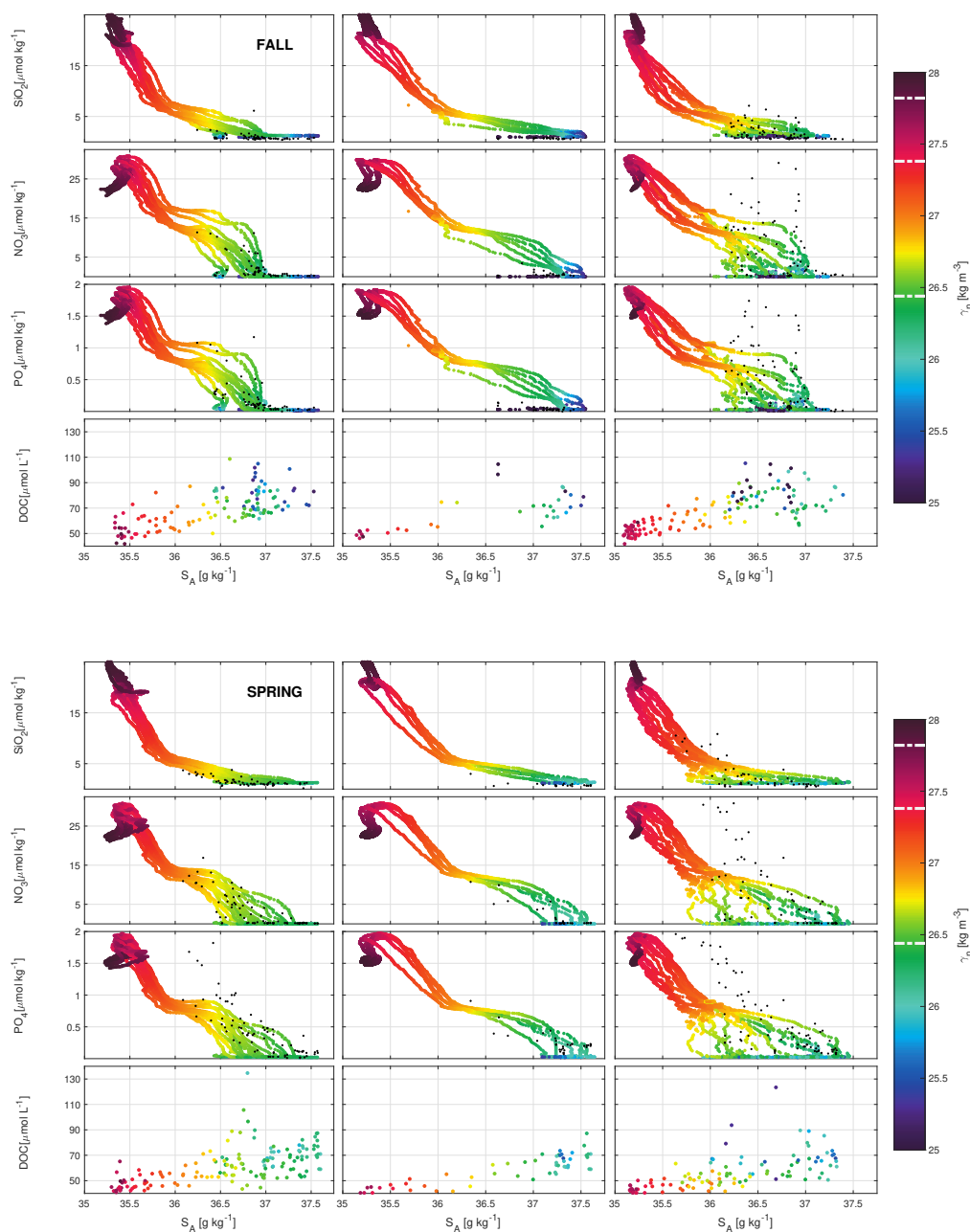
Figure 6. Scatter plots for SiO_2, NO_3 and PO_4 nutrients ($\mu mol\,kg^{-1}$ extracted from GLORYS-BIO), and for DOC (observational data in $\mu mol\,L^{-1}$) with respect to S_A and γ_n at the north (left), west (middle) and south transects (right) in fall (top) and spring (bottom). The isoneutrals 26.44, 27.38 and 27.82 $kg\,m^{-3}$ that limit the waters layers are indicated with white dashed lines in the colorbar. The measured IN concentrations ($\mu mol\,kg^{-1}$) for SiO_2, NO_X and PO_4 until 250 m depth are included as black dots.
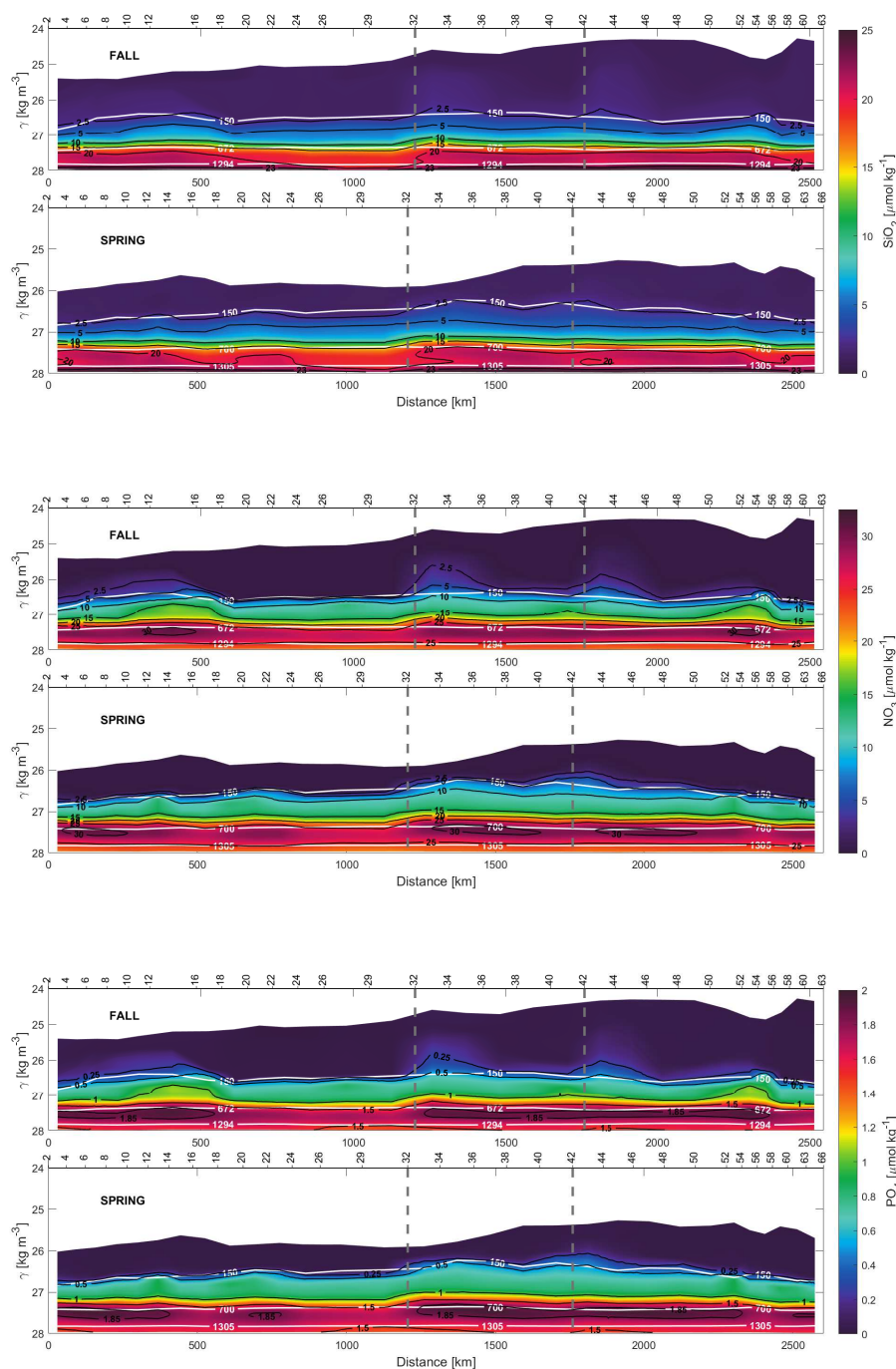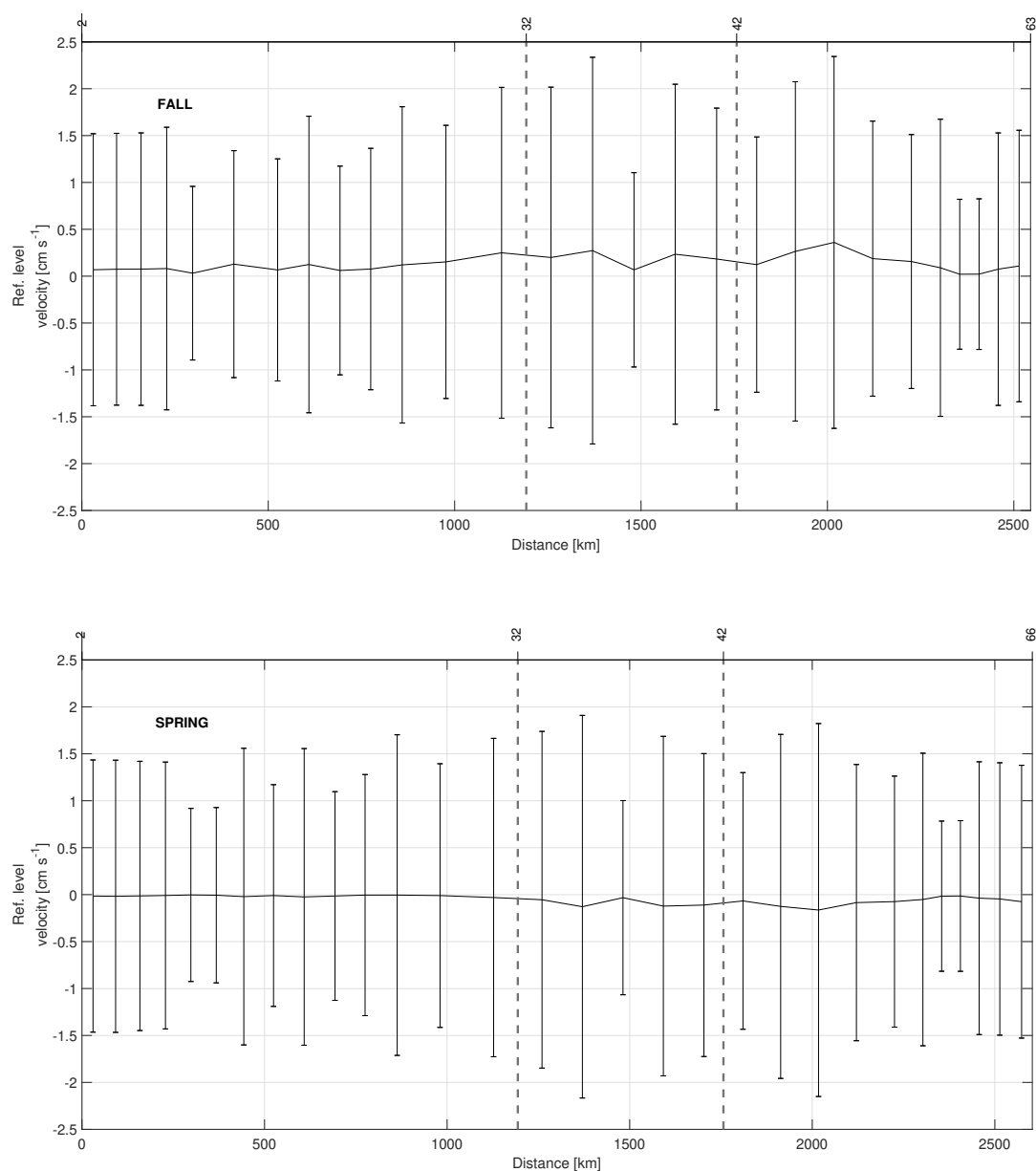
Figure 7. Sections for SiO_2 (top), NO_3 (middle) and PO_4 (bottom) concentrations with respect to γ_n during fall (top) and spring (bottom) extracted from GLORYS-BIO. The white isolines as in the γ_n sections of Figs. 4 and 5.
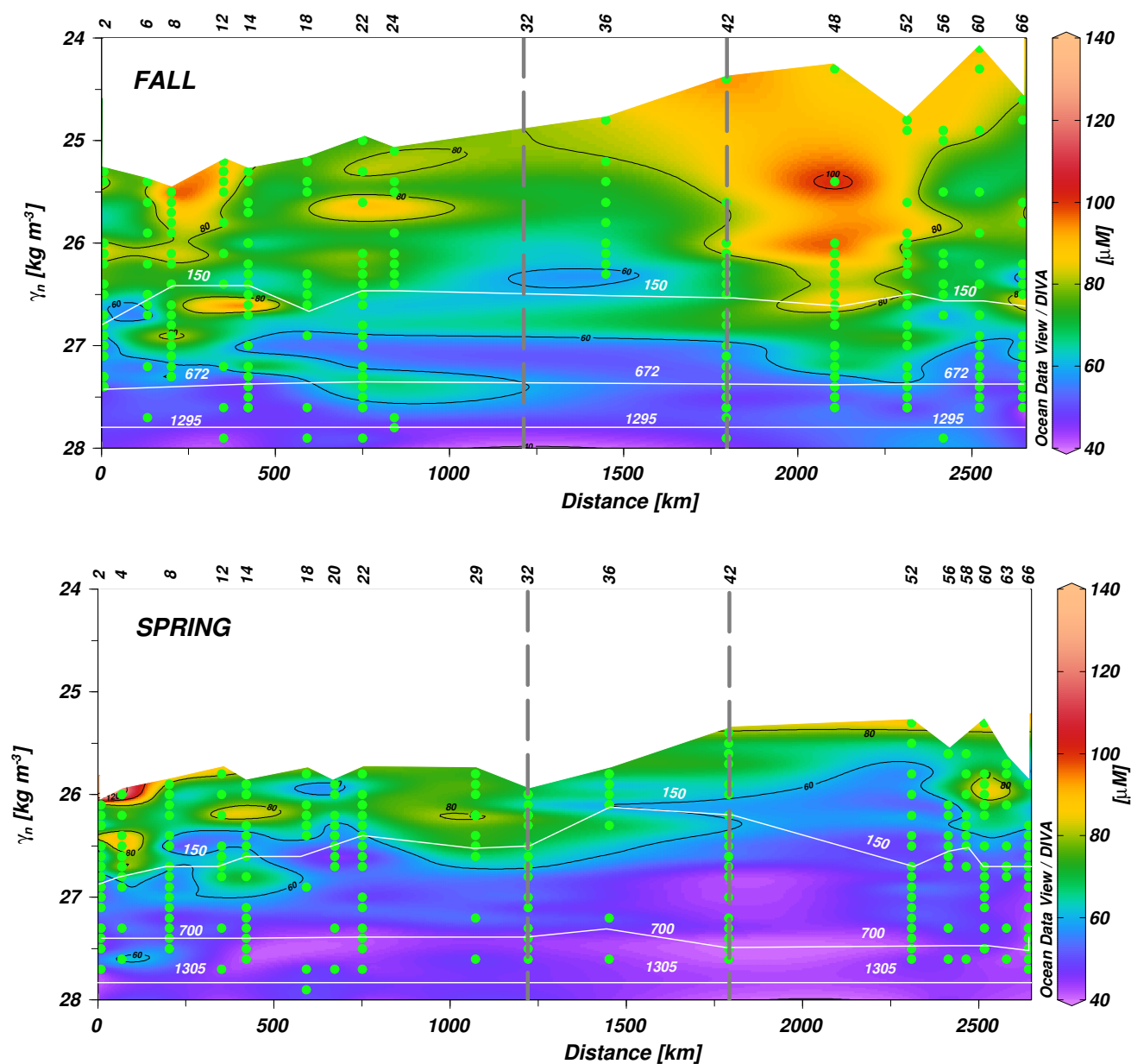
Figure 8. Sections of DOC concentration with respect to γ_n during fall (top) and spring (bottom) cruises with the white isolines as in the γ_n sections of Figs. 4 and 5.

Figure 9. Reference level velocity at $27.962 \, \mathrm{kg \, m^{-3}}$ and its standard deviation estimated by the inverse model during fall (top) and spring (bottom). The direction chosen for the representation is the same as in Fig. 2. The signs of the velocity are according to the geographical criterion, i.e., the velocities are positive/negative toward north/south, in the northern and southern transects and they are positive/negative toward east/west in the western transect.

Ocean Science
Discussions
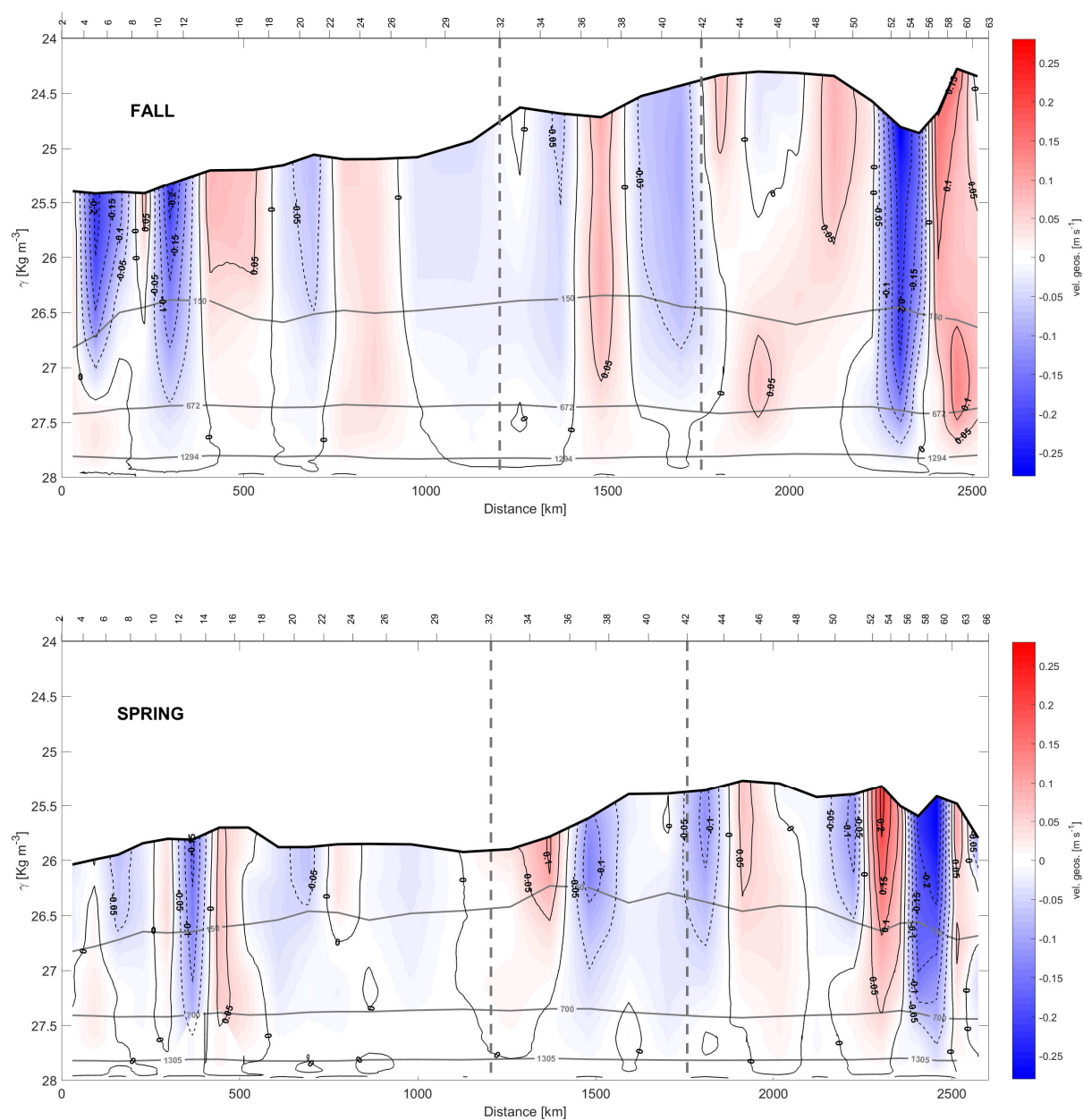
Figure 10. Sections of the absolute geostrophic velocity with respect to γ_n during fall (top) and spring (bottom). The horizontal axis has the same direction as Figure 2 and the criterion of the velocity signs is as in Figure 9. The depths 150, 672/700 and 1204/1305 m are highlighted by grey isolines as in the γ_n sections of Figures 4 and 5.
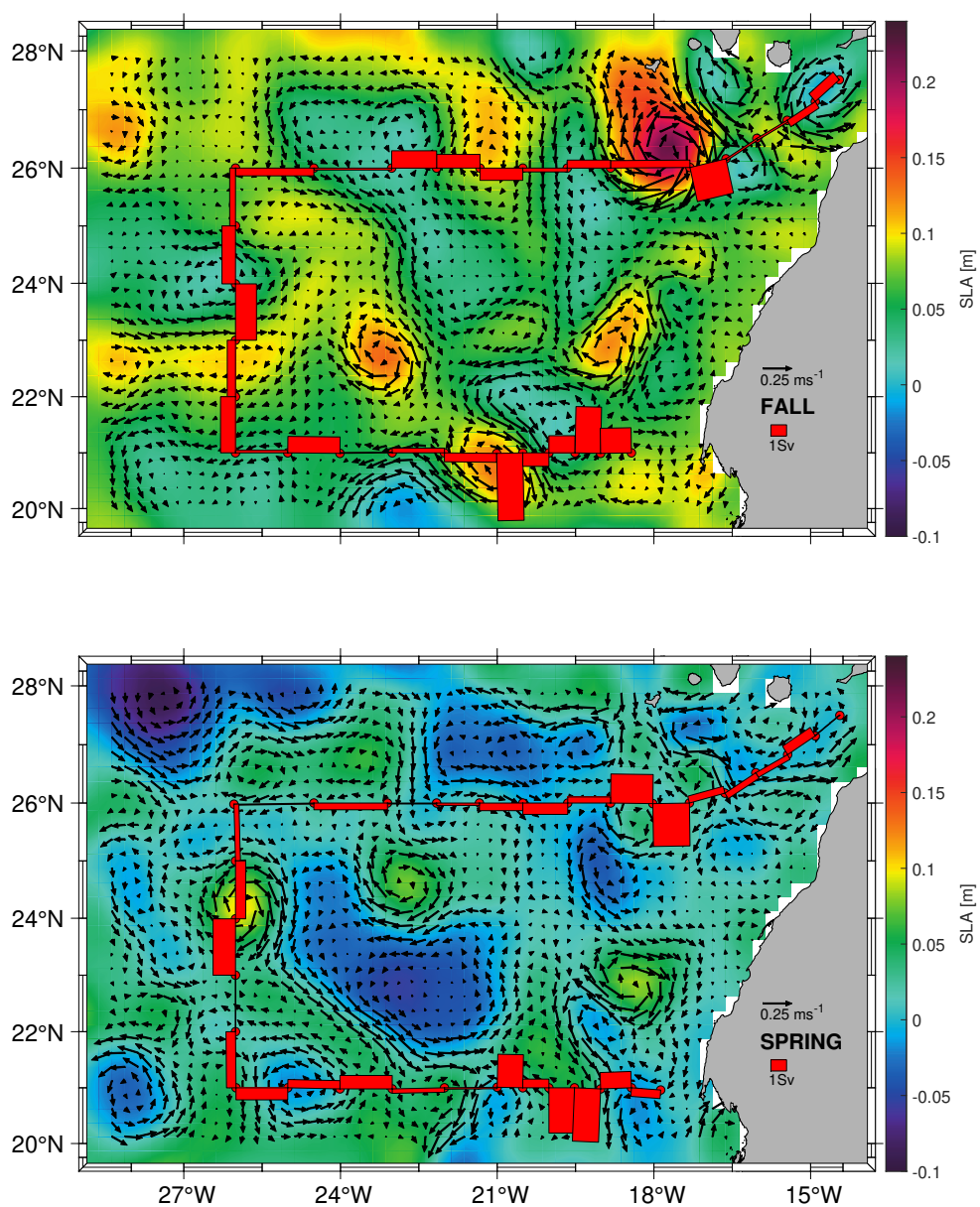
Figure 11. Average derived geostrophic velocity and SLA during fall (top) and spring (bottom) extracted from AVISO+. The red bars represent the mass transports in the shallowest layer as estimated by the inverse model.
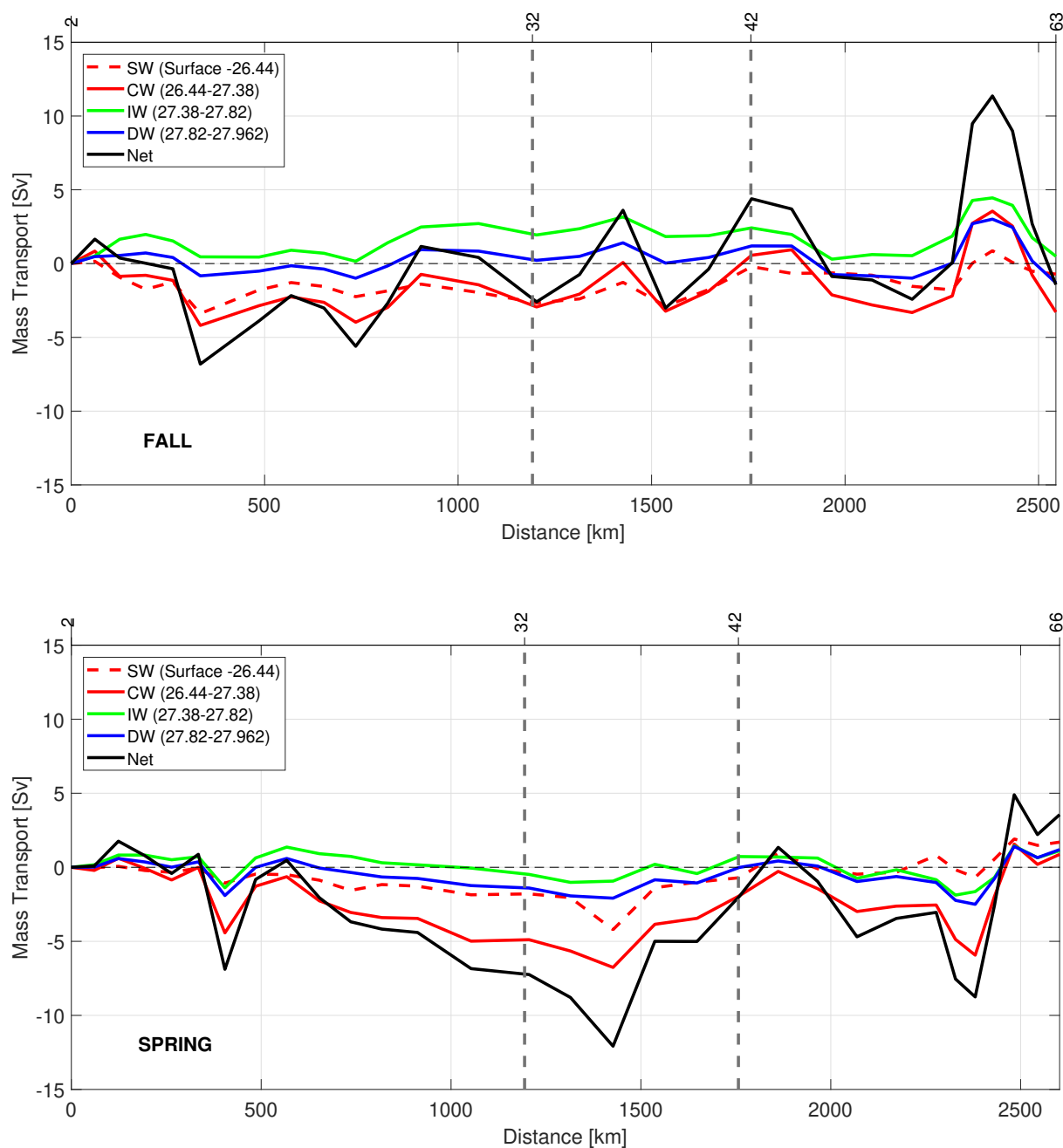
Figure 12. Accumulated mass transport along the fall (top) and spring (bottom) cruises at surface waters (SW, in red and dashed line), central waters (CW, in red line), intermediate waters (IW, in green line) and deep waters (DW, in blue line). The accumulated mass transport integrated for all the nine layers is also represented. The horizontal axis has the same direction as Fig. 2. Negative/positive values of transports along the three transects indicate inward/outward transports of box delimited by the three transects and the African coast.
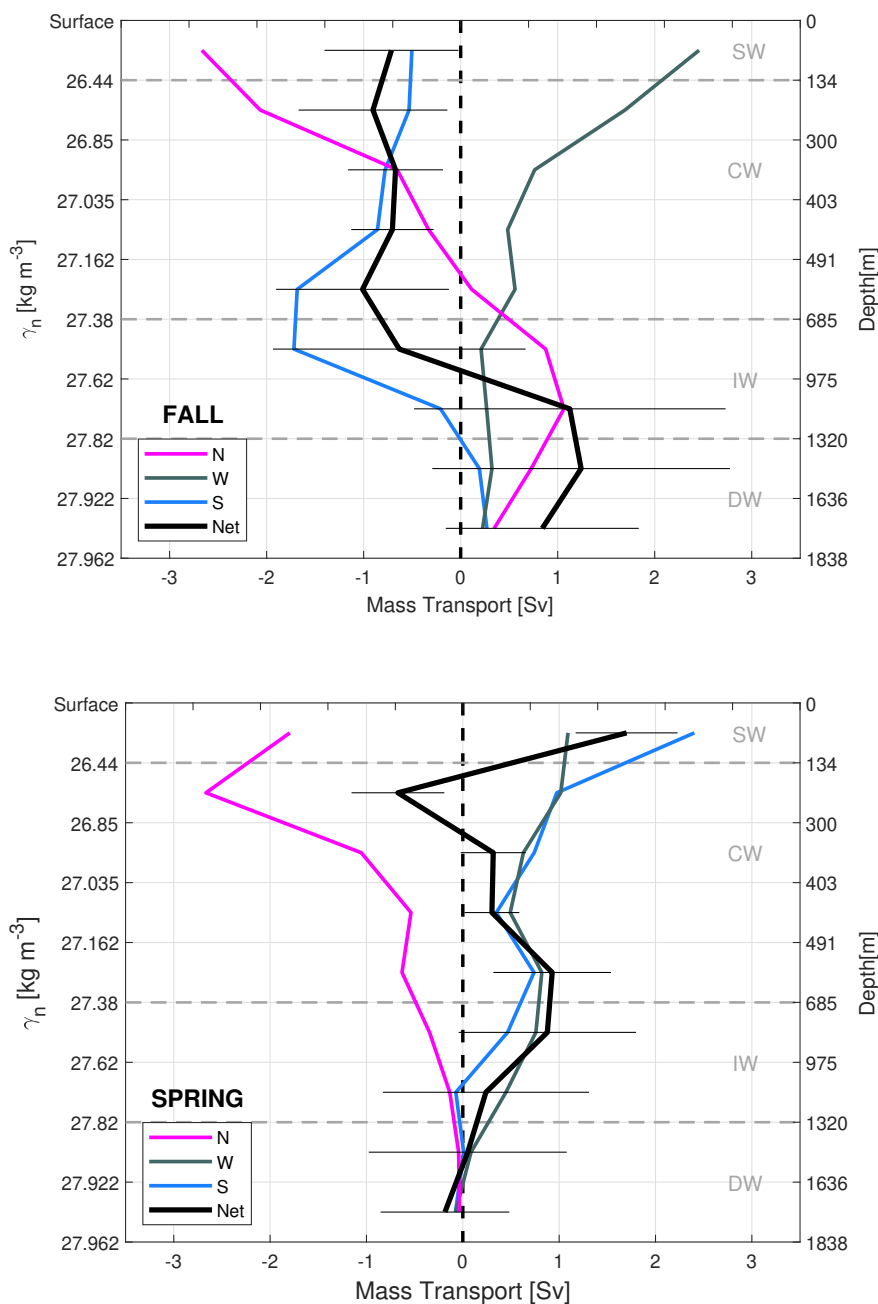
Figure 13. Accumulated mass transports per transect at north (N, magenta line), west (W, dark grey line) and south (S, blue line) transects during fall (top) and spring (bottom). SW transport corresponds to transports between surface and the isoneutral $26.44 \, \mathrm{kg \, m^{-3}}$, CW transport between the isoneutrals 26.44 and $27.38 \, \mathrm{kg \, m^{-3}}$, IW transport between the isoneutrals 27.38 and $27.82 \, \mathrm{kg \, m^{-3}}$ and DW transport between the isoneutrals 27.82 and $27.962 \, \mathrm{kg \, m^{-3}}$. Negative/positive values indicate inward/outward transports as in Fig. 12. Mass conservation in the whole domain is shown by the black line. The horizontal bars represent the uncertainties estimated by the model.
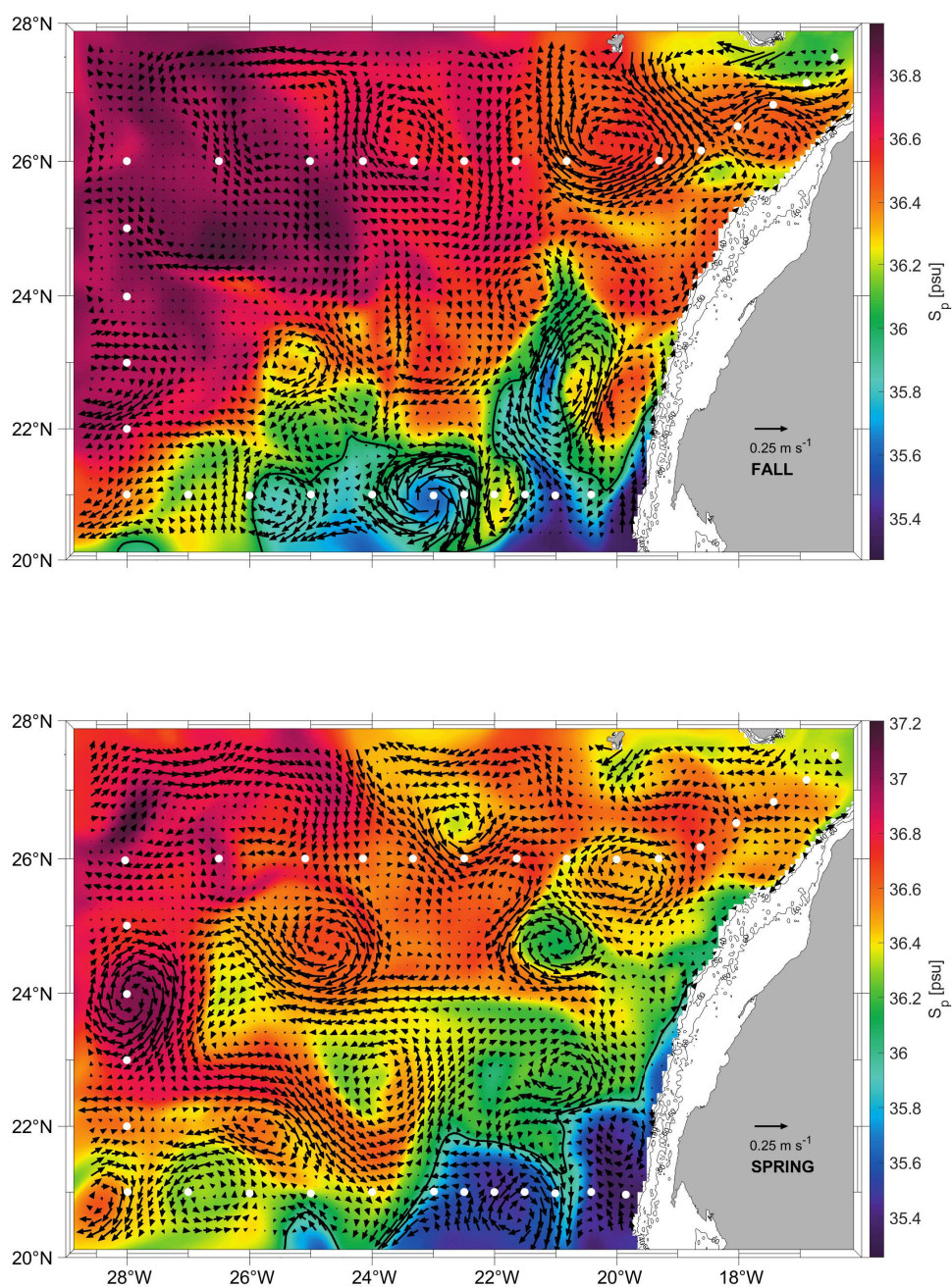
Figure 14. Mean salinity and mean geostrophic velocity at 156 m extracted from GLORYS during fall (top) and spring (bottom). The hydrological sampling stations are represented in white dots and the black line indicates the position of the isohaline of 36 at this depth, used to identify the CVFZ.
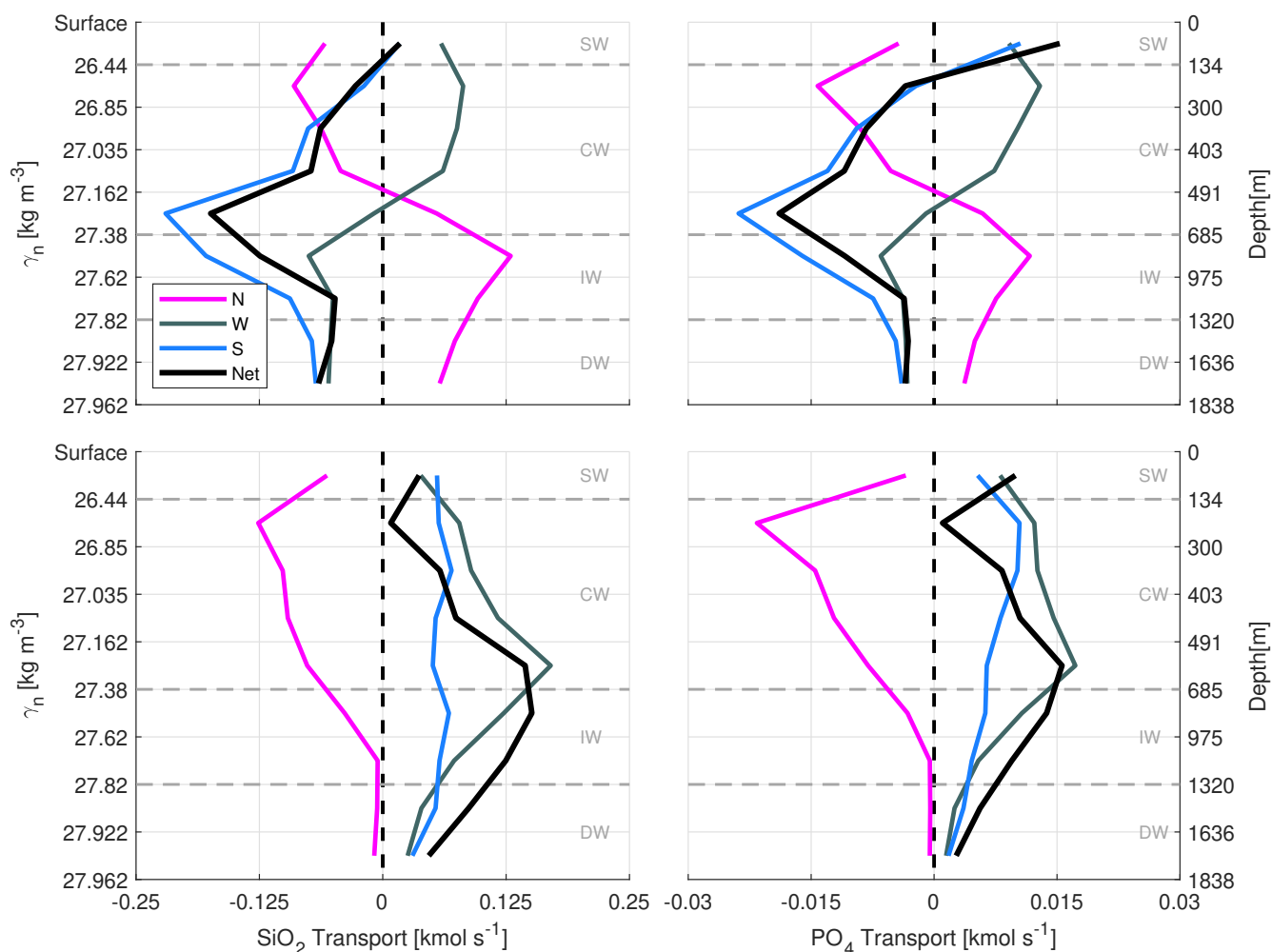
Figure 15. Accumulated SiO_2 and PO_4 transports ($\mathrm{kmol\,s^{-1}}$) at transects north (N, magenta line), west (W, dark grey line) and south (S, blue line) during fall (top) and spring (bottom). SW transport corresponds to transports between surface and the isoneutral $26.44\,\mathrm{kg\,m^{-3}}$, CW transport between the isoneutrals 26.44 and $27.38\,\mathrm{kg\,m^{-3}}$, IW transport between the isoneutrals 27.38 and $27.82\,\mathrm{kg\,m^{-3}}$ and DW transport between the isoneutrals 27.82 and $27.962\,\mathrm{kg\,m^{-3}}$. Negative/positive values indicate inward/outward transports as in Fig. 12. The net transport in the whole box is shown by the black line.
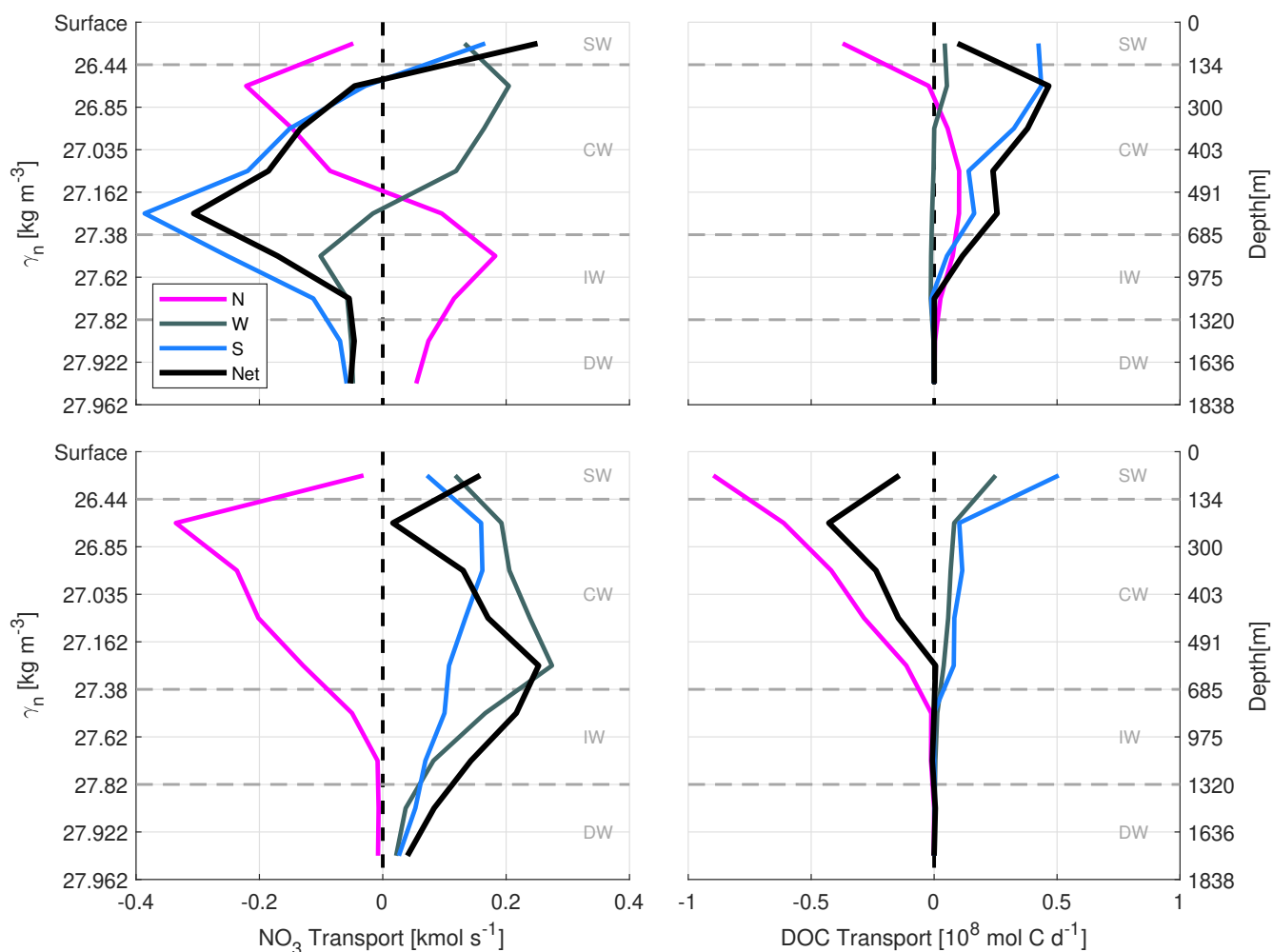
Figure 16. Accumulated NO_3 transports ($kmol\,s^{-1}$) and accumulated DOC transports ($10^8\,molC\,d^{-1}$) at transects north (N, magenta line), west (W, dark grey line) and south (S, blue line) during fall (top) and spring (bottom). SW transport corresponds to transports between surface and the isoneutral $26.44\,kg\,m^{-3}$, CW transport between the isoneutrals 26.44 and $27.38\,kg\,m^{-3}$, IW transport between the isoneutrals 27.38 and $27.82\,kg\,m^{-3}$ and DW transport between the isoneutrals 27.82 and $27.962\,kg\,m^{-3}$. Negative/positive values indicate inward/outward transports as in Fig. 12. The net transport in the whole box is shown by the black line.
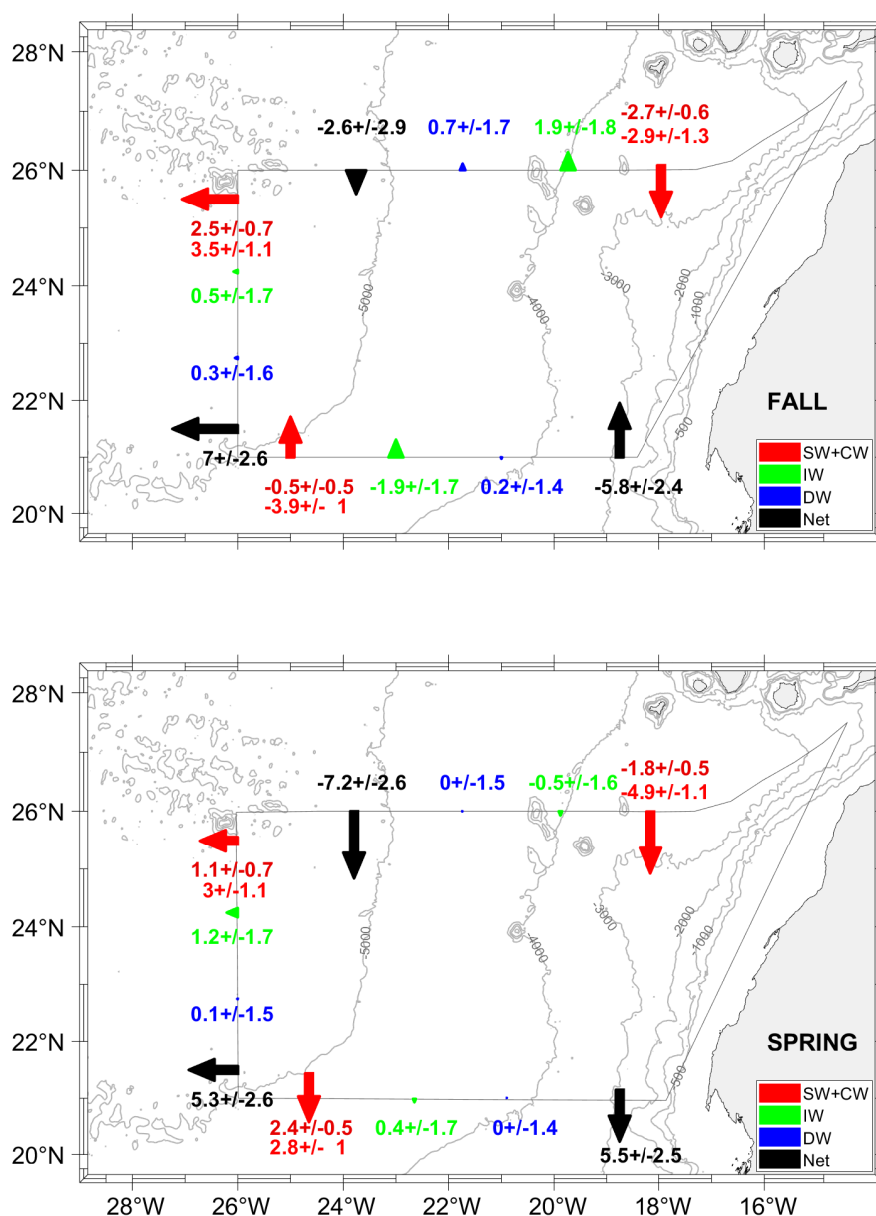
Figure 17. Mass transports with their errors (Sv) at surface and central waters (SW+CW, red arrow), intermediate waters (IW, green arrow) and deep waters (DW, blue arrow) across every transect during fall (top) and spring (bottom). Negative/positive values indicate inward/outward transports as in Fig. 12. The arrows in each transect are located in positions which optimize their visibility, representing the integrated transports along each transect. The values of transports at SW (dark red) are given next to the integrated values of transports at CW levels (in red). The red arrows represent the integrated transports for SW plus CW layers.

Table 1. Summary of the number and type of measurement in stations per transect and season.

SEASON [Cruise]	Type of measurement	Number of stations			
		North	West	South	Total
FALL [COCA-I]	CTD	14	6	11	29
	IN	8	2	6	14
	DOC	8	2	6	15
SPRING [COCA-II]	CTD	15	6	12	31
	IN	9	3	8	18
	DOC	10	3	7	18

Ocean Science
Discussions

Open Access

EGU

Table 2. Summary of water levels (CW, IW, and DW) with their isoneutral limits and their water masses properties for both seasons from the sea surface to 2000 m. The properties extracted from observations are *in situ* temperature (T), potential temperature (θ), conservative temperature (Θ), practical salinity (S_P), absolute salinity (S_A), and dissolved organic carbon (DOC). IN extracted from GLORYS-BIO are silicates (SiO_2), nitrates (NO_3) and phosphates (PO_4).

WATER LEVELS		CW			IW			DW	
γ_n		MIN.		MAX.	MIN.		MAX.	MIN.	MAX.
[kg m^{-3}]		26.44		27.38	27.38		27.82	27.82	27.962
WATER MASSES		NACW		SACW	MW		AAIW	NADW	
PROPERTIES	SEASON	MIN.	MAX.	MIN.	MAX.	MIN.	MAX.	MIN.	MAX.	MIN.	MAX.
T	FALL	9.12	19.13	8.22	17.18	6.03	10.02	5.25	9.12	3.63	5.66
[°C]	SPRING	5.90	19.76	8.35	17.14	6.01	10.04	5.16	9.41	3.63	5.57
θ	FALL	9.04	19.11	8.14	17.16	5.90	9.94	5.13	9.05	3.46	5.53
[°C]	SPRING	5.77	19.74	8.27	17.13	5.88	9.96	5.06	9.34	3.47	5.45
Θ	FALL	9.03	19.05	8.13	17.12	5.89	9.92	5.12	9.03	3.46	5.53
[°C]	SPRING	5.77	19.67	8.26	17.09	5.88	9.94	5.05	9.32	3.47	5.44
S_P	FALL	35.23	36.83	35.04	36.19	35.13	35.44	34.92	35.24	34.99	35.13
	SPRING	33.85	37.06	35.07	36.16	34.55	35.53	34.96	35.30	34.99	35.12
S_A	FALL	35.40	37.00	35.21	36.36	35.30	35.61	35.09	35.40	35.16	35.30
[g kg^{-1}]	SPRING	34.02	37.23	35.24	36.33	34.72	35.70	35.13	35.47	35.16	35.30
SiO_2	FALL	1.24	18.46	6.39	22.14	13.23	21.73	17.50	25.78	18.94	28.44
[µmol kg^{-1}]	SPRING	1.22	21.99	6.99	23.95	13.97	21.99	17.97	28.06	19.04	28.73
NO_3	FALL	0.00	30.27	22.03	36.15	23.13	30.92	25.82	36.36	20.55	28.26
[µmol kg^{-1}]	SPRING	0.00	30.36	25.21	36.75	23.78	31.18	25.70	36.81	21.06	27.97
PO_4	FALL	0.03	1.90	1.46	2.29	1.43	1.98	1.69	2.33	1.37	1.85
[µmol kg^{-1}]	SPRING	0.03	1.90	1.69	2.36	1.49	1.98	1.69	2.39	1.42	1.83
DOC	FALL	47.85	108.65	49.05	74.13	46.25	66.09	41.83	59.30	41.82	58.72
[µM]	SPRING	41.66	105.62	40.86	63.45	40.44	65.15	40.44	50.17	40.44	50.81

Ocean Science
Discussions

Open Access

EGU

Table 3. *A priori* noise of equations corresponding to SW, CW, and DW levels where the different water masses are transported.

WATER LEVELS	UNCERTAINTIES (Sv^2)
SW and CW	$(1.6 - 4.7)^2$
IW	$(6.3 - 9.3)^2$
DW	$(4.0 - 7.9)^2$

Table 4. Mass transports with their errors (Sv) for SW, CW, IW, and DW across north, west, and south transects for both seasons. Positive/negative values indicate outward/inward transports. The last row is the integrated transport for all the water column in each transect while the fourth column summarizes the imbalances in mass transport for both seasons.

WATER LEVELS	SEASON	NORTH	WEST	SOUTH	IMBALANCE
SW	Fall	-2.67 ± 0.60	2.46 ± 0.66	-0.50 ± 0.45	-0.71 ± 1.00
	Spring	-1.80 ± 0.49	1.09 ± 0.69	2.40 ± 0.53	1.70 ± 0.99
CW	Fall	-2.94 ± 1.26	3.50 ± 1.09	-3.85 ± 1.03	-3.29 ± 1.95
	Spring	-4.89 ± 1.14	2.96 ± 1.06	2.80 ± 1.02	0.87 ± 1.86
IW	Fall	1.94 ± 1.85	0.48 ± 1.71	-1.93 ± 1.69	0.49 ± 3.03
	Spring	-0.48 ± 1.65	1.21 ± 1.68	0.39 ± 1.73	1.1 ± 2.92
DW	Fall	0.73 ± 1.71	0.32 ± 1.56	0.19 ± 1.37	1.24 ± 2.69
	Spring	-0.04 ± 1.54	0.09 ± 1.53	0.00 ± 1.42	0.05 ± 2.59
TOTAL	Fall	-2.59 ± 2.88	6.99 ± 2.64	-5.82 ± 2.45	-1.43 ± 4.61
	Spring	-7.24 ± 2.57	5.27 ± 2.60	5.53 ± 2.52	3.55 ± 4.44

Ocean Science
Discussions

Table 5. SiO$_2$ transports and their errors $(\mathrm{kmol\,s^{-1}})$ for CW, IW, and DW for north, west and south transects. Positive/negative values indicate outward/inward transports. The last row is the integrated transport in all the water column in each transect and the last column represents the net transport for this variable inside the box.

WATER LEVELS	SEASON	NORTH	WEST	SOUTH	IMBALANCE
SW	Fall	-0.06 ± 0.01	0.06 ± 0.02	0.02 ± 0.02	0.02 ± 0.02
	Spring	-0.06 ± 0.02	0.04 ± 0.02	0.06 ± 0.01	0.04 ± 0.02
CW	Fall	-0.14 ± 0.06	0.21 ± 0.06	-0.41 ± 0.11	-0.34 ± 0.20
	Spring	-0.40 ± 0.09	0.45 ± 0.16	0.23 ± 0.08	0.28 ± 0.61
IW	Fall	0.23 ± 0.22	-0.13 ± 0.45	-0.27 ± 0.24	-0.17 ± 1.07
	Spring	-0.04 ± 0.15	0.19 ± 0.27	0.12 ± 0.55	0.28 ± 0.72
DW	Fall	0.13 ± 0.31	-0.11 ± 0.52	-0.14 ± 1.00	-0.12 ± 0.25
	Spring	-0.01 ± 0.51	0.06 ± 1.15	0.08 ± 13.38	0.13 ± 6.79
TOTAL	Fall	0.16 ± 0.17	0.03 ± 0.01	-0.80 ± 0.34	-0.61 ± 1.97
	Spring	-0.51 ± 0.18	0.75 ± 0.37	0.49 ± 0.22	0.73 ± 0.91

Ocean Science
Discussions

Open Access

EGU

Table 6. NO_3 transports and their errors $(\mathrm{kmol\,s^{-1}})$ for CW, IW, and DW for north, west and south transects. Positive/negative values indicate outward/inward transports. The last row is the integrated transport in all the water column in each transect and the last column represents the net transport of this variable inside the box.

WATER LEVELS	SEASON	NORTH	WEST	SOUTH	IMBALANCE
SW	Fall	-0.05 ± 0.01	0.13 ± 0.04	0.17 ± 0.15	0.25 ± 0.35
	Spring	-0.03 ± 0.01	0.12 ± 0.07	0.07 ± 0.02	0.16 ± 0.09
CW	Fall	-0.36 ± 0.15	0.47 ± 0.15	-0.78 ± 0.21	-0.67 ± 0.40
	Spring	-0.90 ± 0.21	0.91 ± 0.33	0.56 ± 0.20	0.57 ± 1.22
IW	Fall	0.30 ± 0.28	-0.16 ± 0.57	-0.36 ± 0.32	-0.23 ± 1.39
	Spring	-0.06 ± 0.20	0.25 ± 0.35	0.17 ± 0.75	0.36 ± 0.94
DW	Fall	0.13 ± 0.30	-0.10 ± 0.48	-0.13 ± 0.91	-0.10 ± 0.21
	Spring	-0.01 ± 0.52	0.06 ± 1.05	0.08 ± 12.63	0.12 ± 6.26
TOTAL	Fall	0.02 ± 0.02	0.35 ± 0.13	-1.11 ± 0.47	-0.74 ± 2.40
	Spring	-1.01 ± 0.36	1.34 ± 0.66	0.88 ± 0.40	1.21 ± 1.51

Table 7. PO_4 transports and their errors $(\mathrm{kmol\,s^{-1}})$ for CW, IW, and DW for north, west and south transects. Positive/negative values indicate outward/inward transports. The last row is the integrated transport in all the water column in each transect and the last column represents the net transport of this variable inside the box.

WATER LEVELS	SEASON	NORTH	WEST	SOUTH	IMBALANCE
SW	Fall	-0.00 ± 0.00	0.01 ± 0.00	0.01 ± 0.01	0.02 ± 0.02
	Spring	-0.00 ± 0.00	0.01 ± 0.01	0.01 ± 0.00	0.01 ± 0.01
CW	Fall	-0.02 ± 0.01	0.03 ± 0.01	-0.05 ± 0.01	-0.04 ± 0.02
	Spring	-0.06 ± 0.01	0.06 ± 0.02	0.04 ± 0.01	0.04 ± 0.08
IW	Fall	0.02 ± 0.02	-0.01 ± 0.04	-0.02 ± 0.02	-0.01 ± 0.09
	Spring	-0.00 ± 0.01	0.02 ± 0.02	0.01 ± 0.05	0.02 ± 0.06
DW	Fall	0.01 ± 0.02	-0.01 ± 0.03	-0.01 ± 0.06	-0.01 ± 0.01
	Spring	-0.00 ± 0.04	0.00 ± 0.07	0.01 ± 0.85	0.01 ± 0.42
TOTAL	Fall	0.00 ± 0.00	0.02 ± 0.01	-0.07 ± 0.03	-0.05 ± 0.15
	Spring	-0.06 ± 0.02	0.08 ± 0.04	0.06 ± 0.03	0.08 ± 0.10

Ocean Science
Discussions

Open Access

Table 8. DOC transports and their errors ($10^8 \, \mathrm{mol\,C\,d^{-1}}$) for CW, IW, and DW for north, west and south transects. Positive/negative values indicate outward/inward transports. The last row is the integrated transport in all the water column in each transect and the last column represents the net transport for this variable inside the box. These values are transports of non-refractory DOC which is obtained by subtracting an amount of $40 \, \mathrm{\mu mol\,L^{-1}}$ from the measured DOC.

WATER LEVELS	SEASON	NORTH	WEST	SOUTH	IMBALANCE
SW	Fall	-0.37 ± 0.08	0.04 ± 0.01	0.42 ± 0.38	0.10 ± 0.13
	Spring	-0.90 ± 0.24	0.25 ± 0.16	0.51 ± 0.11	-0.14 ± 0.08
CW	Fall	0.24 ± 0.10	0.04 ± 0.01	1.06 ± 0.28	1.34 ± 0.80
	Spring	-1.43 ± 0.33	0.25 ± 0.09	0.38 ± 0.14	-0.80 ± 1.72
IW	Fall	0.10 ± 0.10	-0.03 ± 0.09	0.04 ± 0.04	0.12 ± 0.72
	Spring	-0.02 ± 0.08	0.02 ± 0.02	-0.00 ± 0.00	-0.01 ± 0.02
DW	Fall	0.00 ± 0.01	-0.00 ± 0.02	-0.00 ± 0.00	0.00 ± 0.00
	Spring	-0.00 ± 0.06	0.00 ± 0.04	0.00 ± 0.58	0.00 ± 0.23
TOTAL	Fall	-0.03 ± 0.03	0.06 ± 0.02	1.53 ± 0.64	1.55 ± 5.01
	Spring	-2.35 ± 0.84	0.52 ± 0.25	0.89 ± 0.40	-0.95 ± 1.19